NOVA SCHOOL OF
SCIENCE & TECHNOLOGY

DEPARTAMENT OF
MATERIALS SCIENCE

CAROLINA ALVES BENTES

BSc in Micro and Nanotechnologies Engineering

DETERMINATION OF MECHANICAL PROPERTIES OF THIN FILM MATERIALS USED IN OXIDE TFTS TOWARD ADVANCED MATERIAL MODELS

MASTER IN MICRO AND NANOTECHNOLOGIES ENGINEERING

NOVA University Lisbon

September, 2022

NOVA SCHOOL OF
SCIENCE & TECHNOLOGY

DEPARTAMENT OF
MATERIALS SCIENCE

DETERMINATION OF MECHANICAL PROPERTIES OF THIN FILM MATERIALS USED IN OXIDE TFTS TOWARD ADVANCED MATERIAL MODELS

CAROLINA ALVES BENTES

BSc in Micro and Nanotechnologies Engineering

Adviser: André Clausner, Ph.D.,
Head of Department, Fraunhofer IKTS

Co-adviser: Pedro Barquinha, Ph.D.,
Associate Professor, NOVA University Lisbon

Examination Committee:

Chair: Rodrigo Martins, Ph.D.,
Full Professor, NOVA University of Lisbon

Rapporteurs: Igor Zlotnikov, Ph.D.,
Group Leader, TU Dresden

Adviser: André Clausner, Ph.D.,
Head of Department, Fraunhofer IKTS

MASTER IN MICRO AND NANOTECHNOLOGIES ENGINEERING

NOVA University Lisbon
September, 2022

Determination of Mechanical Properties of Thin Film Materials Used in Oxide TFTs Toward Advanced Material Models

Dedicatory lorem ipsum.

ACKNOWLEDGEMENTS

As a first remark, I wish to show my appreciation to Professor Elvira Fortunato and Professor Rodrigo Martins for paving the way that allowed me to pursue my studies in the Micro and Nanotechnology Degree.

I want to talk to everyone at that I crossed paths at *Fraunhofer IKTS,* for being extremely supportive and welcoming me so well in such a good team environment, with a special thank you note to my advisor Dr. André Clausner, for enduring with me until the last moment, raising my morale when needed and tutoring me. I also want to thank Sylvia Conzendorf for the FIB-SEM cross-sections, Christoph Sander for the FEM simulations, Juliane Posseckardt for the EDS analysis and Wieland Heyn for teaching me the ways of the nanoindenter and helping me when in trouble with the software.

Quero também agradecer ao meu coorientador, o Prof. Dr. Pedro Barquinha, por ter estado presente para me tirar dúvidas e acompanhar os resultados, mesmo estando eu noutro país. Agradeço também à Ana Santa do CEMOP, por me ajudar com a fabricação das amostras, com os melhores votos de maternidade.

Numa nota pessoal, quero agradecer à minha mãe e ao pai, pois sem o apoio deles, nada disto teria sido possível, e ao meu irmão pela frase inspiradora "As teses não se acabam, entregam-se". Agradeço a todos os meus colegas e amigos, que fizeram parte do meu percurso académico, especialmente à Sofia por ser a minha predileta companhia de estudo na Biblioteca de Cascais e à Amanda pelo suporte que me deu ao longo destes anos em diversos aspetos.

This work received funding from the European Community's H2020 program, Grant Agreements No. 716510 (ERC-2016-StG TREND), and 952169 (SYNERGY, H2020-WIDESPREAD-2020-5, CSA)

“Neue Wege entstehen, indem wir sie gehen!.” (Nietzsche).

ABSTRACT

With an increasing demand for improvement and innovation in the field of microelectronics, flexible electronics, driven by applications that range from displays to medical devices, has gained much relevance in recent years. Thin film transistors (TFTs) are the main building block for flexible microelectronic systems, but a better understanding of the mechanical properties of the constituent thin film materials is necessary to design more reliable microelectronic devices to be used in mechanically harsh environments. This work aims to extract a set of mechanical properties of thin film materials used in flexible oxide TFTs and based on that, parameterize material models for Finite Elements Analysis (FEA).

To acquire data for these material models, films from different materials are fabricated on silicon substrates. For assessing the impact of thickness and annealing process on the mechanical properties of the thin films, several samples of the same material are fabricated with distinct specifications. This study is divided into two workflows for extracting two distinct sets of parameters. For films composed of metals (Mo), semiconductors (IGZO) and dielectrics (Ta_2O_5 and Ta_2O_5/SiO_2), the hardness and, as the main parameter, Young´s modulus, are determined by nanoindentation for describing linear elasticity. For the polymeric films (PI), time-dependent parameters such as storage modulus, loss modulus and phase angle, which are necessary to describe viscoelasticity, are determined by nanoscale Dynamic Mechanical Analysis (nano-DMA).

Based on these experimental results, the linear elastic and viscoelastic material models are parameterized for the Finite Element Method (FEM). Based on these FEM models, now relevant geometries could be simulated. Beyond that, following the methodology of the dissertation, further thin films used in oxide TFTs could be characterized which paves the way for the acquisition of data from other relevant materials and the obtaining of a complete description of the device for product development.

Keywords: flexible electronics, thin films, mechanical properties, oxide TFTs, material function, finite element modelling.

RESUMO

Com uma procura crescente por melhoria e inovação no ramo da microeletrónica, a eletrónica flexível, impulsionada por aplicações que vão desde displays a dispositivos médicos, tem vindo a ganhar muita relevância nos últimos anos. Transístores de filme fino (TFTs) são o principal bloco de construção para sistemas microeletrónicos flexíveis. Mas uma melhor compreensão das propriedades mecânicas dos materiais constituintes de filme fino é necessária para projetar dispositivos microeletrónicos mais confiáveis para serem utilizados em ambientes mecanicamente desafiadores. Este trabalho visa extrair um conjunto de propriedades mecânicas de materiais de filmes finos usados em TFTs de óxidos flexíveis e, com base nestas, parametrizar modelos de materiais para Análise de Elementos Finitos.

Para adquirir dados para esses modelos de materiais, filmes de diferentes materiais são fabricados em substratos de silício. Para avaliar o impacto de espessura e do processo de recozimento nas propriedades mecânicas dos filmes, várias amostras são fabricadas com especificações distintas. Este estudo é dividido em dois fluxos de trabalho para a extração de dois conjuntos distintos de parâmetros. Para filmes compostos de metais (Mo), semicondutores (IGZO) e dielétricos (Ta_2O_5 e Ta_2O_5/SiO_2), a dureza e, como parâmetro principal, o módulo de Young, são determinados por nanoindentação para descrever a elasticidade linear. Para os filmes poliméricos (PI), parâmetros dependentes do tempo, como o módulo de armazenamento, o módulo viscoso e o ângulo de fase, necessários para descrever a viscoelasticidade, são determinados por Análise Mecânica Dinâmica em nanoescala (nano-DMA).

Com base nesses resultados experimentais, modelos de materiais lineares elástico e viscoelástico são parametrizados para o Método dos Elementos Finitos (MEF). Com base nesses modelos MEF, geometrias relevantes podem agora ser simuladas. Além disso, seguindo a metodologia da dissertação, outros filmes finos usados em TFTs de óxidos podem ser caracterizados, o que abre caminho para a aquisição de dados de outros materiais relevantes e a obtenção de uma descrição completa do dispositivo para o desenvolvimento de produtos.

Palavras chave: eletrónica flexível, filmes finos, propriedades mecânicas, TFTs de óxido, função do material, modelagem de elementos finitos.

CONTENTS

LIST OF FIGURES

LIST OF TABLES

ACRONYMS

TFT	Thin Film Transistor.
CENIMAT	Centro de Investigação de Materiais.
i3N	Instituto de Nanoestruturas, Nanomodelação e Nanofabricação.
IKTS	Institut für Keramische Technologien und Systeme.
FEM	Finite Element Method.
AEF	Análise de Elementos Finitos.
MEF	Método dos Elementos Finitos.
RFID	Radio Frequency Identification Devices.
CdS	Cadmium Sulphide.
SI	Amorphous Silicon.
OTFT	Organic Thin Films Transistor.
IGZO	Indium-Gallium-Zinc-Oxide.
PI	Polyimide.
DMA	Dynamic Mechanical Analysis.
FE	Finite Element.
CEMOP	Centro de Excelência de Microeletrónica e Optoeletrónica de Processos.
CZ	Czochralski.
RF	Radio Frequency.
PVD	Physical Vapour Deposition.
IPA	Isopropyl Alcohol.
FIB	Focused Ion Beam.
SEM	Scanning Electron Microscope.
SPM	Scanning Probe Microscopy.
EDS	Energy Dispersive X-Ray Spectroscopy.
ISE	Indentation Size Effect.
TSM	Thermorheologically Simple Materials.
WLF	Williams-Landel-Ferry.
BC	Boundary Condition.

SYMBOLS

A	Contact area.
a_T	Shift factor.
A_p	Projected contact area.
β	Indenter geometry constant.
c_i	Indenter damping.
c_s	Sample damping.
C_1	Material constant.
C_2	Other material constant.
δ	Phase angle or phase lag.
E	Young's modulus.
E^*	Complex modulus.
E_i	Indenter's Young´s modulus.
E_s	Sample's Young's modulus.
E_r	Reduced Young´s modulus.
$E_r^{'}$	Reduced storage modulus.
$E_r^{''}$	Loss modulus.
ε	Strain.
h	Displacement.
H	Hardness.
h_c	Displacement at permanent hardness impression.
h_f	Displacement after the indenter is fully unloaded.
h_0	Displacement of linearly extrapolating the initial portion of the unloading curve to zero loads.
h_{max}	Displacement at peak load.
k_i	Indenter stiffness.
k_s	Sample stiffness.
ν	Poisson´s ratio.
ν_i	Indenter Poisson´s ratio.

$\boldsymbol{\nu_s}$	Sample Poisson's ratio.
$\boldsymbol{P}$	Indentation load.
$\boldsymbol{P_{max}}$	Peak load.
$\boldsymbol{\pi}$	The ratio of the circumference of a circle to its diameter, having a value rounded to eight decimal places of 3.14159265.
$\boldsymbol{S}$	Initial unloading contact stiffness.
$\boldsymbol{\sigma}$	Stress.
$\boldsymbol{T}$	Temperature.
$\boldsymbol{T_r}$	Reference temperature.
Tan $\boldsymbol{\delta}$	Damping – the tangent of the phase angle.
$\boldsymbol{\omega}$	Applied frequency.

MOTIVATION AND OBJECTIVES

Thin films can be used for a variety of applications in the field of electronics. In recent years, there has been increased interest, particularly in flexible electronics drawing much attention from governments, industry, and academia. This translated into a boom of research progress, with a rich library of flexible devices being reported raging from integrated circuit components to environment-interactive units. One of the main challenges that come from flexible devices is to make them mechanically robust, reliable, and durable when under mechanical stress.

For this reason, this study focuses on a detailed mechanical characterization of thin films used in flexible oxide thin-film transistors (oxide TFTs) being developed at *CENIMAT-i3N*. All the experimental work was done at *Fraunhofer IKTS*, in the framework of the *SYNERGY Project* (Symbiosis for Energy Harvesting Concepts for Smart Platforms on Foil) with funding from the European Union's Horizon 2020 Research and Innovation Programme (Grant Agreement No. 952169).

The main objectives of the work are:

- Determination of the mechanical properties of thin films used for oxide TFT fabrication at i3N-CENIMAT
- Definition of the material model in ANSYS

Because the materials in this study exhibit distinct mechanical behaviour, the two workflows shown in Figure 0.1 were established to determine the mechanical properties of the thin films. For materials that exhibit linear-elastic behaviour, the experimental work consists of nanoindentation quasi-static measurements, while for those exhibiting viscoelastic behaviour, nanoscale dynamic mechanical analysis (nano-DMA) was performed.

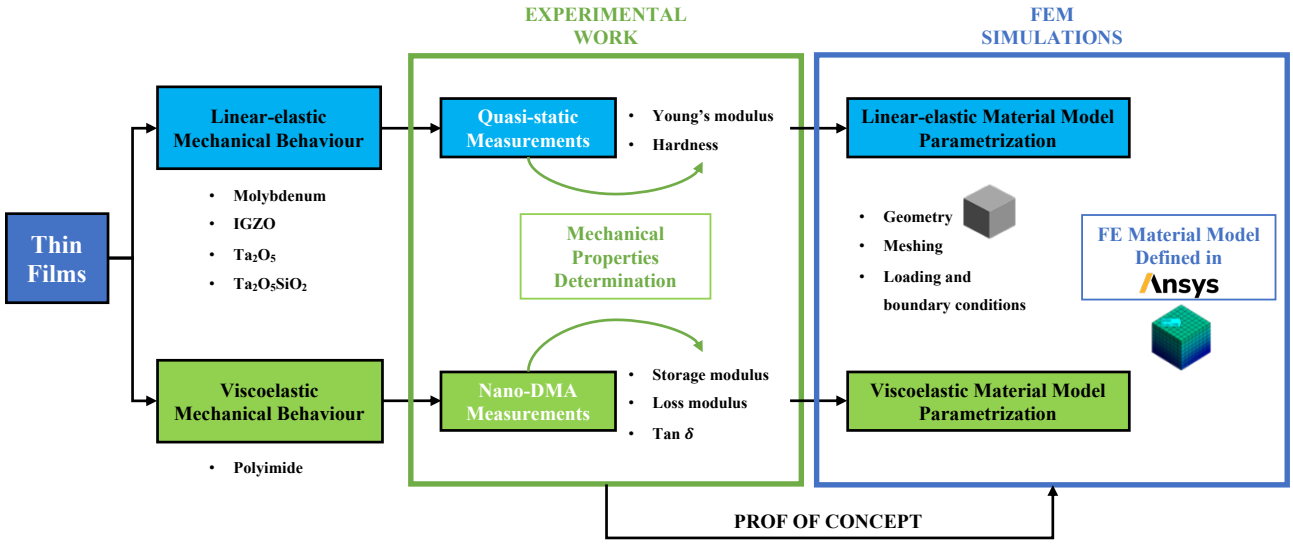

Figure 0.1 — Schematic representation of the workflows established to achieve the objectives of this study.

Hence, the respective material models were defined in ANSYS, proving the concept that the materials parameters obtained from challenging measurements, can be transferred to a FEM material model. Material models and simulation tools are fundamental to eliminate trial-and-error loops during the development of TFT devices,

as they allow the illustration of complex load scenarios and make predictions of the behaviour of the constituent thin film materials. Thus, this work paves the way for the simulation of complete TFT structures and, consequentially, for an improvement in the design of such devices. Ultimately, this will contribute to overcoming one of the main challenges in flexible electronics, reliability.

1

INTRODUCTION

1.1 Thin Films in Flexible Electronics

Thin films have been used in several applications in microelectronics (e.g., transistors, sensors, coatings, energy devices, memories) mostly due to their versatility and an extensive variety of fabrication processes. These thin film devices are designed with outstanding mechanical deformability, sensitivity to multifunctional responses, and intelligent control capabilities. One of the main driving forces in thin film technology is flexible electronics because it offers many applications in multiple fields such as flexible circuits[1, 2], flexible displays[3–8], electronic paper,[9, 10] wearable devices[11–13], medical devices,[14] conformable radio frequency identification devices (RFID)[15–17] and electronic skin for robots[18–22].

1.1.1 Thin Film Transistors (TFTs)

The most common thin-film electronic device is the thin film transistors (TFTs) that poses the foundation for flexible platforms. The first TFTs were initially proposed in 1962[23] and were based on cadmium sulphide (CdS). In 1979, silicon-based TFTs were developed and are nowadays widely used in flat panel displays. A TFT stack is shown in Figure 1.1 and it compromises metals, dielectrics, semiconductors, and a flexible substrate. Due to their inherent flexibility, TFTs made from many different types of thin film materials have been studied such as flexible amorphous silicon (a-Si)[24, 25] to organic thin films transistors (OTFTs). However, in

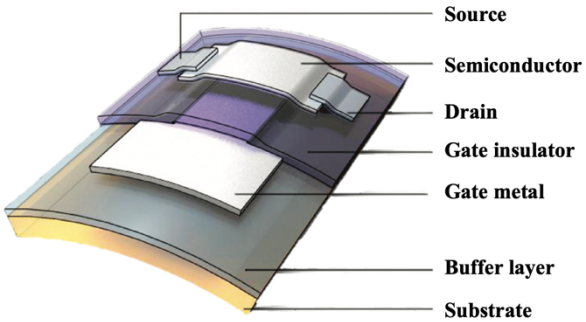

Figure 1.1 — Schematic representation of a TFT structure on a flexible substrate. The architecture represented here is a bottom-gate top-contact transistor.[34]

the case of OTFTs, these exhibit relatively low mobility and stability.[26, 27] Oxide-based TFTs, particularly those based on multicomponent oxide semiconductors, such as amorphous indium-gallium-zinc-oxide (a-IGZO), can be considered one of the main breakthroughs in the field of flexible electronics, as they pose several advantages when compared to conventional amorphous silicon. They were first introduced in 2004,[28] exhibiting low process temperature, high carrier mobility, good uniformity, and high transparency in the visible regions.[28–32] Research has shown that the electronic properties of amorphous oxide semiconductors are also particular insensitive to mechanical strain.[17, 33] From a mechanical point of view, the most resilient semiconductor, in which flexibility is permitted, is the amorphous IGZO, characterized by an absence of grain boundaries and a unique conduction-band structure, allowing therefore high electron mobility and good insensitivity

to mechanical strain.[28, 34] To achieve flexible devices, the substrate material must be bendable. These can be composed of polymer plastics,[17, 28, 35] paper sheets,[36–39] metal foils,[40, 41] and flexible thin glass.[42–44] Polymer plastics have many advantages as the choice of flexible substrate, namely high transparency, stretchability, lightweight and bendability.[28, 45–48] The most commonly used plastic substrate for oxide TFTs is polyimide (PI).[22, 35, 49–53] For gate insulators in the TFT structure, there are several choices of dielectric materials. Materials like Al_2O_3,[54] HfO_2[55] or Ta_2O_5[56] that have a high dielectric constant (high-κ)[57] are the main choice of materials for low-temperature sputtering processes. Nonetheless, they still pose some challenges, namely a low-band offset with IGZO resulting in relatively large gate leakage current[57–59] which have been addressed by a multi-component approach. This consists of using as dielectrics, compositions of thin films such as Ta_2O_5/SiO_2 and Ta_2O_5/Al_2O_3 that have been shown to significantly improve the electrical performance of TFT devices.[60] As for the source, drain and gate, metals such as Al, Cu, Ti and Mo[61] are commonly chosen as good candidates, as they show good electrical conductivity, adequate workfunction for ohmic contacts with most n-type oxide semiconductors, easy processability (deposition and etching) and low-to-moderate costs.

Most research on the characteristics of TFTs focuses mainly on the electrical properties, with only limited emphasis given to the mechanical aspects of these devices. For this reason, it is very important to study the impact of mechanical stress on the flexible device performance. In this field, the existing literature is mostly directed toward understanding what happens to the device when it comes under compressive and tensile strain[62], how it impacts its electrical performance[62, 63], and how to optimize its structure and device layout.[64–66] Nevertheless, reports on determination of mechanical properties of the thin films composing the TFT stack are scarce, being precisely one of the main objectives of this work.

1.2 Mechanical Properties of Thin Films

Thin films ranging in thickness from a few nanometres to a few micrometres, compromise the structure of the TFTs used in flexible electronics. These are frequently subjected to very large stresses which can cause a wide variety of deformation and fracture processes to occur. While thin films are extremely thermally stable and reasonably hard, they are still fragile. The mechanical properties of thin films often differ from those of bulk materials. For these reasons, it is important to understand the mechanical properties of the constituent layers of the devices so that these can be more reliable, structural integral, and capable of maintaining that integrity over their lifetime. In this study, the most important mechanical properties are the ones that define the elastic region, as can be seen in Figure 1.2, namely the Youngs modulus, given that after mechanical stress, thin film devices must be restored to their initial form. For many materials, the relationship between stress and strain can be expressed, at least at low strains, by Hooke´s law which states that stress is proportional to strain, (linear elasticity). This enables us to define the Young´s modulus, E,[67] of a material which for simple uniaxial extension or compression is given by

$$E = \sigma/\varepsilon \tag{1.1}$$

In the case of polymeric materials, these do not obey Hooke's law because their response to applied stress or strain depends upon the rate or time period of loading. Polymers are termed viscoelastic as they display both viscous behaviour at high temperatures and low rates of strain, and elastic behaviour at low temperatures and high rate of strain.[68] For this reason, to achieve a mechanical characterization of polymers, creep rate, viscosity, and damping must be considered. For the study of viscoelastic materials, it is fundamental

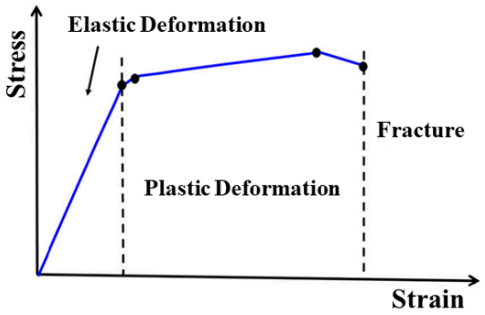

Figure 1.2 — Stress vs strain of a material.

to get an understanding of the viscoelastic polymer properties, such as the storage modulus, loss modulus and loss tangent (tan δ or phase angle).

1.2.1 Fundamentals of Nanoindentation

Nanoindentation has become one of the most important techniques used to determine the mechanical properties of thin films. This is because the properties of the film can be measured without removing the film from the substrate; the spatial distribution of properties, in both lateral and depth dimensions, can be measured; the tests can be performed quickly and inexpensively; and it is a versatile technique.[69] The most commonly adopted method for measuring hardness and modulus using nanoindentation consists of making a small indentation in the film, usually with a *Berkovich* indenter, while simultaneously recording the indentation load, P, and displacement, h, during one complete cycle of loading and unloading.[70, 71] A schematic of load versus depth from the nanoindentation test using a *Berkovich* pyramid-shaped tip indenter is shown in Figure 1.3 (a). The quantities involved in the analysis are the peak load, P_{max}, the displacement at peak load, h_{max}, the permanent depth of penetration after the indenter is fully unloaded, h_f, the initial unloading contact stiffness, $S = \mathrm{d}P/\mathrm{d}h$ (i.e., the slope of the initial portion of the unloading curve, and the displacement found by linearly extrapolating the initial portion of the unloading curve to zero loads, h_0). The procedure used to measure Young's modulus and hardness is based on the unloading processes shown schematically in Figure 1.3 (b).

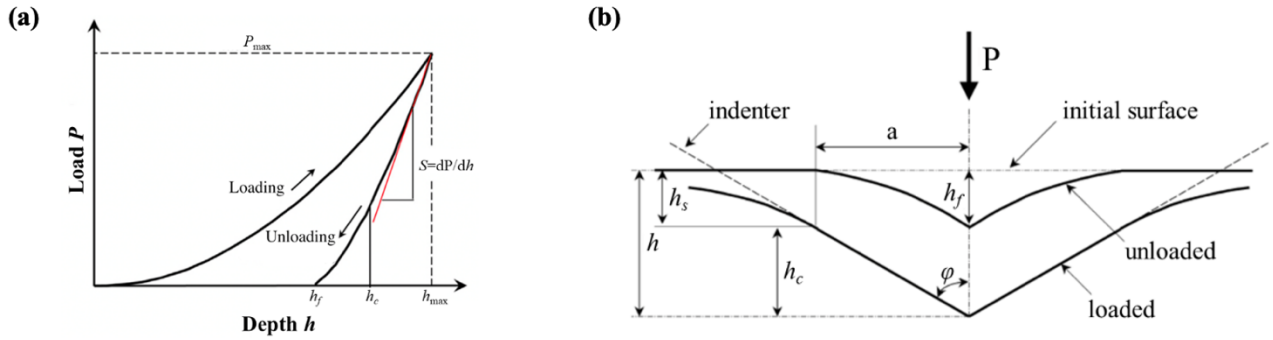

Figure 1.3 — (a) A schematic representation of load versus indenter displacement data for an indentation experiment. (b) A schematic illustration of the unloading process showing parameters characterizing the contact geometry.

Elastic and plastic deformation occurs as the indenter is first driven into the film. The plastic deformation results in the formation of a permanent hardness impression that conforms to the shape of the indenter to some contact depth, h_c. Also, the surface displaces downward at the edge of the contact by an amount, h_s. The analysis procedure focuses on the fact that as the indenter is withdrawn, the elastic displacements are recovered, and an analysis of the elastic unloading data can then be used to relate experimentally measured quantities to the projected contact area, A, and an effective elastic modulus.[72, 73] For any axisymmetric indenter, the relationship is

$$S = \frac{dP}{dh} = \frac{2}{\sqrt{\pi}} E_r \sqrt{A} \tag{1.2}$$

The Young´s modulus of the specimen, E, is obtained by the following equation

$$\frac{1}{E_r} = \frac{1-\nu^2}{E} + \frac{1-\nu_i^2}{E_i} \tag{1.3}$$

where E_i and ν_i are Young´s modulus and Poisson´s ratio of the diamond indenter, respectively; ν is the Poisson´s ratio of the specimen; E_r the reduced Young´s Modulus. A calibration procedure is necessary to acquire the precise shape of the indenter which is required to determine the hardness and modulus. For a *Berkovich* indenter with a perfect triangular pyramid geometry, the area function is given by $F(d) = 24.5h_c^2$, however, no real indenter is perfect, and it is needed to consider the tip rounding effect, especially for small indentations. One of the methods to establish the area function consists in making several indentations in a material with well-known, isotropic elastic properties, such as fused quartz or sapphire, and the area function is deduced from the indentation load-displacement data by assuming that the elastic constants are independent of depth.[71] The reduced modulus is given by

$$E_r = \frac{S}{2\beta} \sqrt{\frac{\pi}{A_p(h_c)}} \tag{1.4}$$

in which S is the stiffness of the specimen; β is a constant on the order of unity that depends on the geometry of the indenter; $A_p(h_c)$ is the projected area of the indentation at the contact depth, h_c, and it is often approximated by a fitting of the polynomial function. The determination of the contact depth[71] is then given by

$$h_c = h_{max} - 0.75P_{max}/S \tag{1.5}$$

and the projected area of contact is thus calculated, and the hardness is given by

$$H = \frac{P_{max}}{A} \tag{1.6}$$

1.2.2 Time-Dependent Nanoindentation: Dynamic Indentation Testing

For time-dependent materials, the viscoelastic parameters cannot be directly measured because the mechanical response is temperature and time-dependent. Nano-DMA is a technique that allows the determination of the viscoelastic properties of the materials with a high local resolution. It consists of applying a pre-load to the indentation experiments, and the determination of the phase shift between an overlayed dynamical force load and the subsequent dynamic displacement reaction. This phase shift is used to calculate the storage and loss modulus.[74] The evaluation of the measurement data is based on a dynamical model of the whole experimental setup that takes into consideration the damping $(c_{s,i})$ and stiffness $(k_{s,i})$ of both the sample and indenter. The viscoelastic polymeric properties (reduced storage modulus, $E_r^{'}$, and loss modulus, $E_r^{''}$) are given by the following relationships:

$$E_r^{'} = \frac{k_s\sqrt{\pi}}{2\sqrt{A}}, E_r^{''} = \frac{\omega c_s\sqrt{\pi}}{2\sqrt{A}} \tag{1.7}$$

where ω is the applied frequency, A the contact area between the sample and indenter tip, determined by experimental calibrations, as well as k_s and c_s that are given from experimental data. Like static indentation measurements, the storage and loss modulus of the sample are both related to the measured reduced modulus and indenter properties by

$$\frac{1}{E_r^{'''}} = \frac{(1-v_i^2)}{E_i^{'''}} + \frac{(1-v_s^2)}{E_s^{'''}} \tag{1.8}$$

where v is the Poisson´s ratio and the subscripts i and s are the indenter and sample properties, respectively. The storage modulus and the loss modulus are related to the complex modulus, $E^* = E^{'} + iE^{''}$, and indicate the ability of the polymer to store and return energy (recoverable deformation) and dissipate energy through molecular chain reactions, such as internal friction and rearrangement of the chain due to deformation. The ratio of the loss modulus to the storage modulus (i.e., tan δ or phase angle) reflects the viscoelastic behaviour of the material and is a useful parameter because it is independent of the tip-sample contact area.

1.2.3 Challenges in the Nanoindentation of Thin Films

The main challenge in the nanoindentation of thin films is avoiding unintentionally probing the properties of the substrate. To minimize this effect, it is common to restrict the maximum depth of penetration to 10% of the film thickness.[71] However, this requires some critical analysis, since this rule does not strictly apply in all cases, due to effects such as tip rounding, thus it is the most generally used since it covers a wide range of material behaviour. For the determination of the elastic modulus, it is not possible avowing the substrate influence since the elastic deflections of both the substrate and the film contribute to supporting the indenter load. Although, more support comes from the film than the substrate given the localized nature of the indentation stress field. The hardness value is more challenging to quantify due to the complex nature of the plastic zone as it interacts with the substrate material. A drop in hardness is expected for small penetration depths, hence the elastic deformation associated with the tip rounding. With sufficient resolution, the hardness values should reach a plateau and this value should represent the film hardness.[75]

1.3 Finite Element Method (FEM)

The Finite Element Method is a powerful numerical technique that uses computation power to calculate approximate solutions to boundary value problems for partial differential equations like here continuum mechanics tasks. It uses the subdivision of a whole problem domain into simpler parts, called finite elements and variational methods from the calculus of variation to solve the problem by minimizing an associated error function. Figure 1.4 describes the fundamentals of a continuum mechanics FEM process. Firstly, it is necessary to define the material models, i.e., specifying the mechanical behaviour present in the FE model. Further, the

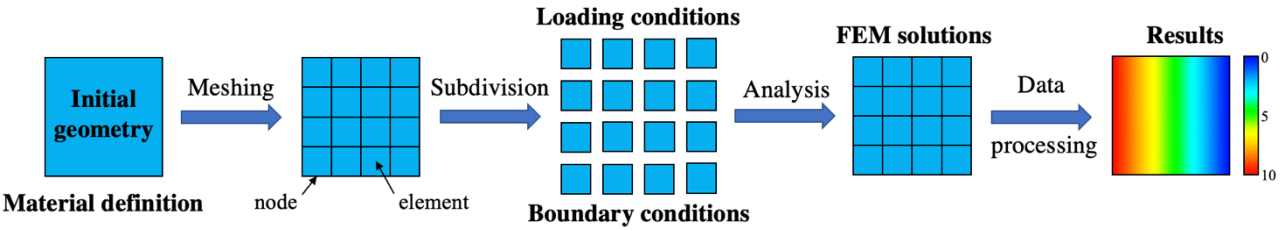

Figure 1.4 — Schematic of the fundamentals of a FEM simulation process.

element types and their properties need to be defined according to the problem to be solved. This is followed by discretization of the sample geometry, where a mesh is defined, separating the sample geometry by nodes into individual elements. Last, the loading and boundary conditions are defined, i.e., specification of the type of loading and constraints. With these definitions, the FEM can be handed over and it is then possible to run

the computation to achieve the FEM solutions of the continuum mechanics problem that then contain results to be analysed (post-processing), e.g., stress-strain fields, displacement fields, etc.

FEM has been extensively used to characterize the mechanical behaviour of bulk materials and thin film geometries by simulating nanoindentation procedures. For indentation processes, the finite element simulation can be employed for investigating the complex stress and strain fields under the indenter tip which is extremely difficult to achieve by experiment. This technique has been applied to metals and polymers.[76, 77]

In this study, the transition of materials data obtained from challenging nano-mechanical experiments to FE material models (linear elastic and viscoelastic) including a proof-of-concept for the full FEM workflow until post-processing using simple geometries have been done.

2

MATERIALS AND METHODS

2.1 Fabrication Process of the Thin Films

Different types of thin films were fabricated in *CEMOP-UNINOVA*'s clean room. Firstly, thin films of molybdenum (Mo), IGZO, tantalum pentoxide (Ta_2O_5) and a double layer of Ta_2O_5 with silicon dioxide (SiO_2), were all fabricated by sputtering, and lastly, thin films of polyimide (PI) were fabricated by spin coating. For films of different specifications, an extra sample was fabricated with a pattern of three rectangles made with a marker, where after deposition, a lift-off process with acetone occurred. The profile for each sample after deposition was then measured.

2.1.1 Materials

The substrates used to deposit all the films were CZ-Si wafers cut in 2.5 by 2.5 cm (thickness of 500 ± 50 μm) obtained from *MicroChemicals*. The molybdenum and IGZO layers were deposited in an RF Magnetron Sputtering PVD AJA ATC 1300F, with the first using a molybdenum target from *AJA International*, and the latest, using three *AJA International* targets with a composition of 2:1:1 (In_2O_3:Ga_2O_3:ZnO molar ratio). An RF Magnetron Sputtering PVD AJA ATC 1800F was used to deposit the Ta_2O_5 and the Ta_2O_5/SiO_2 multilayer using a Ta_2O_5 target and a SiO_2 target for the latest, with both targets from *AJA International*. The polyimide thin films were fabricated by spin-coating in a *SUSS LabSpin6* with PI 2610 (for 500 nm and 1 μm) and PI 2611 (for 10 μm) with the adhesion promoter VM652 (PI and adhesion promoter from *HD MicroSystems*™).

2.1.2 Molybdenum and IGZO Thin Films

For all the samples, the substrates were cleaned by ultrasonic baths of 15 min each, firstly in acetone followed by IPA. The drying process was done afterwards with a nitrogen gun.

Different deposition times were used to achieve a variation in film thickness between samples. Mo was deposited in an Ar (50 sccm) atmosphere with a power of 175 W and pressure of 1.7 mTorr. For IGZO, the atmosphere was Ar + O (20:5 sccm), with a power of 143 W for In_2O_3, 100 W for Ga_2O_3 and 50 W for ZnO, at a pressure of 2.3 mTorr. In Table 2.1, can be observed an outline of the respective deposition time regarding the desired film thickness.

After the deposition, for each sample and respective thickness, three different thermal treatments were performed: no annealing, annealing at 180 °C and 300 °C. The annealing was done on a hot plate for 1h for each temperature.

2.1.3 Ta_2O_5 and Multilayer Stack Thin Films

For the multilayer stack and single Ta_2O_5 layer, the deposition was conducted under the same conditions, being an Ar+O (14:1 sccm) atmosphere, power of 100 W for Ta_2O_5 and 200 W for SiO_5, and pressure of 2.3 mTorr.

For the desired thickness of 350 nm, the Ta_2O_5 was deposited for 20 min. The samples corresponding to the individual layer were removed and the SiO_2 deposition for the multilayer samples proceeded. The SiO_2 deposition time was 88 min.

Table 2.1 — Deposition time for molybdenum and IGZO concerning the desired film thickness.

Sample	Desired Thickness (nm)	Deposition Time (min)
Mo	100	17
	200	34
	500	84
IGZO	100	30
	200	60
	500	150

This deposition was followed by the same thermal treatments that were done for the Mo and IGZO thin films.

2.1.4 Polyimide Thin Films

Polyimide thin films were formed on the rigid silicon wafer by spin-coating liquid PI. An aminosilane-based adhesion promoter was applied before the liquid to enhance the adhesion to the silicon substrate. All samples were spin-coated in two steps, with the first being the same for all samples and consisting of spinning for 7 s at 500 rpm. To obtain a thickness of 10 µm, a speed up to 1500 rpm for 30 s was applied, for 1 µm, 4000 rpm for 30 s, and for 500 nm, 6000 rpm for 30 s. The soft bake was carried out at 90 °C for 1 min and 30 s, and an initial curing at 150 °C for 1 min and 30 s.

In similarity to the previous samples, three different annealing processes were done: no annealing, annealing of 250 °C for 1 h and annealing of 350 °C for 30 min. Higher temperatures are important for complete curing of PI films.[78–80]

2.2 Characterization Techniques

2.2.1 Thickness Measurements: Profilometer and FIB-SEM

The measurement of the deposition thicknesses was done with the Profilometer *Dektak 3* available at *CEN-IMAT-i3N*. For the samples Ta_2O_5 as deposited (without annealing) and Ta_2O_5/SiO_2 as deposited, additional thickness measurements were performed with *Zeiss NVision 40* FIB-SEM at *Fraunhofer IKTS*, to get a second assessment and determine if the quality of the film was adequate for the following work.

2.2.2 Mechanical Characterization: Nanoindentation

The mechanical characterization of all samples was performed by nanoindentation at *Fraunhofer IKTS*, using the *Hysitron TI 950 Triboindenter* from *Bruker*. This technique allows the measuring of hardness and elastic modulus as well as viscoelastic parameters for the fabricated samples. A pyramidal-shaped diamond *Berkovich* indentation tip from *Synton-MDP* was chosen to perform all nanoindentation measurements. A high-precision

transducer from *Hysitron* allowed the monitoring of loads and displacements with a resolution down to less than 30 nN and 0.2 nm, respectively. The test instrument and the tip was calibrated following the approach proposed by Oliver and Pharr.[81] To accomplish the objectives of this work, two distinct nanoindentation tests were performed: quasi-static measurements to obtain the elastic modulus and hardness, and nanoscale dynamic mechanical analysis (nano-DMA) to give insight into the viscoelastic behaviour of the polyimide.

For the quasi-static measurements, load is applied in a series of steps to some maximum and then withdrawn. Simultaneously, the indenter force and displacement are recorded and analysed to determine the elastic modulus and hardness. For all films, the nanoindentation indents were performed with a minimum load of 100 µN and a maximum load of 10000 µN, in an array of 10 × 10 with a spacing of 20 µm. The load function was 5 s loading time, 5 s creep time, and 5 s unloading time. Yet, for the polyimide samples, the loading time was 10 s, with a creep time of 20 s, and 10 s of unloading time. Before the indentation of the Mo and IGZO samples, in-situ scanning probe microscopy (SPM) images were taken of the indentation sites to get a better understanding of the sample's topography and respective roughness before indents. These scans consisted of a 5 × 5 µm array at a line scan speed of 0.5 Hz.

The dynamic measurements, follow the experimental methodology described by Clausner et al.[82] with a specifically engineered sample adapter, Figure 2.1. The dynamic load was 20 µN while the static load is 2000 µN. The dynamic indentation loads were increased monotonically from 1 Hz to 300 Hz and the sweep consisted of 20 frequencies. However, frequencies until 1 Hz were excluded from the study since they are more prone to drift and would significantly increase the testing time. For statistic proposes, four indents on different test locations were made on all samples for each test temperature. To combine the data of the four measurements into one single group, mathematical analysis was done by decomposing the means and standard deviation.[83]

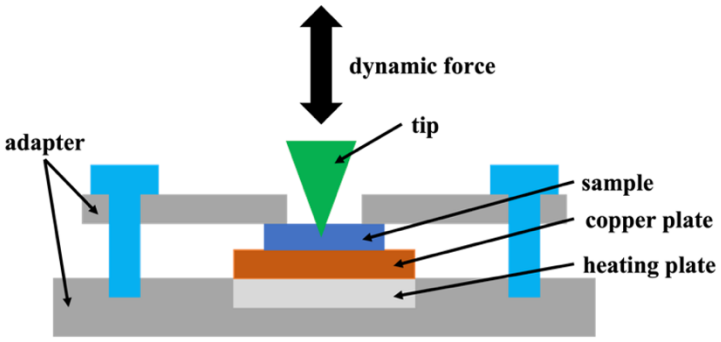

Figure 2.1 — A schematic of the nano-DMA setup used to measure the viscoelastic properties. Adapted from Clausner et al.[82]

2.2.3 Morphological Characterization with EDS-SEM

Due to substantial morphological alterations evaluated by in-situ SPM images of the Mo sample with a thickness of 439 nm annealed at 300 ºC, the chemical composition of was evaluated by EDS-SEM with the *Bruker Xflash®5010 Detector* and *Zeiss NVision 40* SEM at *Fraunhofer IKTS.*

2.2.4 Finite Element Simulations (FEM) with ANSYS

The finite element simulations were performed using the commercial FEM software ANSYS version 2022 R2. As the whole FEM workflow is in the state of a proof-of-concept in this study, a simple cube geometry, as well as a simple set of boundary conditions (displacement-governed cube compression), have been used to

create a minimal functional FE model. In the processing of the force, displacement and stress reactions in the simple cubes have been analysed. The focus of this study was on the transition of the experimentally measured micro-mechanical materials' behaviour to the FEM material model needed for the whole FEM workflow. To that, for the films governed by Hooke's law, such as the Mo and IGZO, a linear-elastic model is used to describe these materials in the FEM code. For polyimide, a viscoelastic material model was used in this study that is analogous to the one described by Slanik et al.[84] These models are directly selected within the ANSYS environment and the Prony Series developed by Park and Schapery[85, 86] are used to describe and implement the viscoelastic behaviour of the PI materials in the FEM code.

3

RESULTS AND DISCUSSION

3.1 Thickness Measurements

The obtained thicknesses do not correspond to the initial desired as can be seen in Table A.1 in Appendix A. However, this was not taken as an issue beforehand. Given that the work intends to acquire a better understanding of how the variation of the thickness of the material impacts its mechanical properties, a difference in thicknesses is already enough to conclude the tendencies observed in the properties. For the polyimide samples, thickness measurements were performed considering the annealing temperature given that polymers are more deeply impacted morphologically[87] by it that the other materials in this study. Therefore, a smaller thickness was expected for a higher annealing temperature, and this can be observed by the data present in this chapter and Table A.1 in the appendix.

Another important factor to be considered when it comes to the nanoindentation technique is surface roughness. A higher roughness in the measured film will have a direct impact on the measurement and lead to errors. To assert the quality of the films, a FIB cut was performed on two samples, and the results in Table 3.1 show that the film is homogeneous with the maximum standard deviation being 4.5 nm for the sample Ta_2O_5/SiO_2 (without annealing). The SEM cross-sections for the Ta_2O_5 sample are present in Figure B.1.1 and Figure B.1.2 and for the Ta_2O_5/SiO_2 sample in Figure B.1.3 and Figure B.1.4, in the Appendix section B.1. Table 3.1, besides presenting the average thickness values for the SEM cross-sections, also compares them with the Profilometer measurements. The difference in values between samples is less than 10%.

Table 3.1 — Comparison of thickness measurements with profilometer and FIB-SEM.

		Profilometer		FIB-SEM	
Material	**Annealing conditions**	**Number of measurements**	**Average thickness (nm)**	**Number of measurements**	**Average thickness (nm)**
Ta_2O_5	No annealing	3	311.9 ± 4.8	8	327.5 ± 3.4
Ta_2O_5/SiO_2	No annealing	3	343.3 ± 4.3	7	381.2 ± 4.5

The profilometer values were the ones considered for this study given that the sample preparation time for FIB-SEM is very extensive and, therefore, not ideal, also from a financial point of view, to be performed on all samples.

3.2 Quasi-Static Measurements

As previously mentioned in Chapter 1, to assess the mechanical properties of thin films composed of metals (Mo), semiconductors (IGZO) and dielectrics (Ta_2O_5 and Ta_2O_5/SiO_2) in the linear elastic region, the quasi-

static nanoindentation technique allows for the extraction of hardness and, most importantly, Young´s modulus of the films. Several depth-depended mechanical property plots were obtained for the nanoindentation measurements, allowing the extraction of the mechanical properties of each film. The indentations were performed until it was achieved a penetration depth of roughly 180 nm which, given the film thicknesses for some samples, will unavoidably probe the substrate properties. For this reason, it is necessary to critically analyse the indentation depth-dependent data and define the depth range in which the signal comes mostly from the thin film. To better assess this and divide it into film and substrate properties, a pre-measurement was done for the silicon substrate on which the films were deposited. This measurement is present in all graphics.

3.2.1 Molybdenum and IGZO Thin Films

Figure 3.1 presents the nanoindentation measurements for the molybdenum film with a thickness of 93 nm. As mentioned in Chapter 1.2.3, there are some considerations to be taken previously when defining the range for the measurement of Young's modulus and Hardness. An effective indentation size range must be found empirically while taking into consideration some effects. For Young's modulus, these effects are mostly far-range and translate into the substrate influence on the measurement. While for the hardness, the effects are mostly short-range and are related to the tip shape. For the left image of Figure 3.1, corresponding to the film without annealing, Indentation Size Effect (ISE) might be present as the hardness is higher at a lower depth, until a penetration depth of 6 nm. ISE is a small-scale phenomenon that translates into an increase in hardness with decreasing penetration depth and becomes important for depths of less than approximately 1 µm.[88] This phenomenon can be attributed to the nucleation of dislocation within the plastic zone.[75]

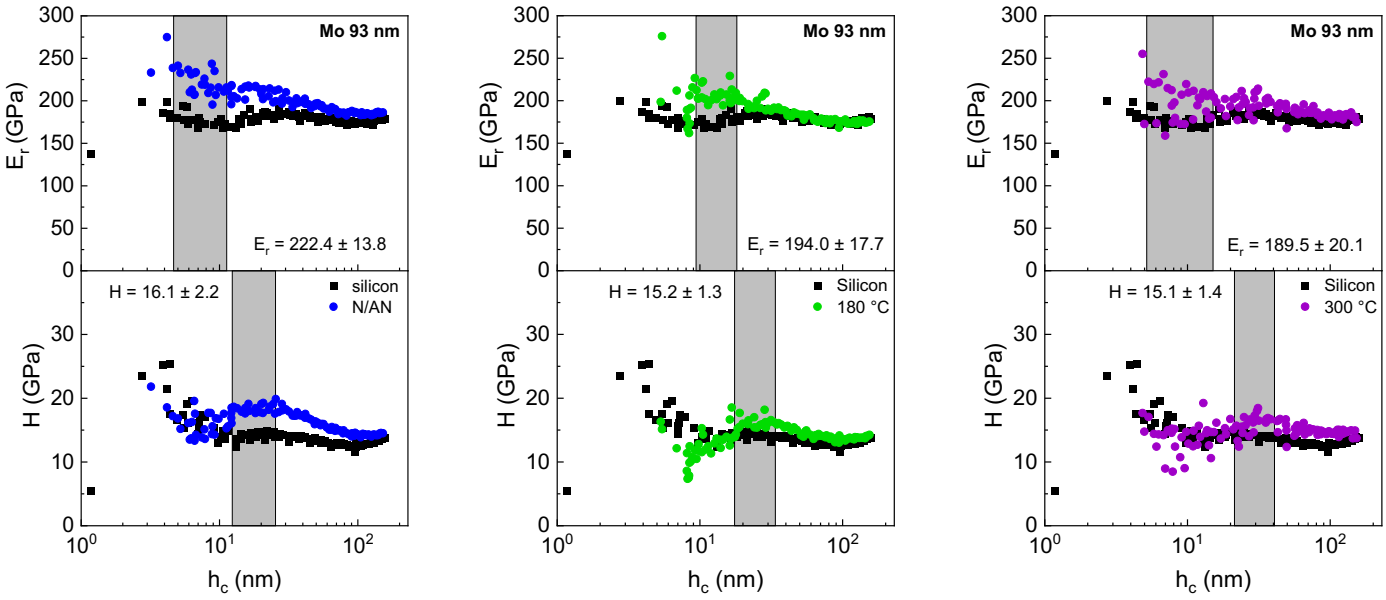

Figure 3.1 — Nanoindentation measurements for Young's modulus and hardness for Mo with a thickness of 93 nm: (left) as deposited; (centre) annealed at 180 ºC; (right) annealed at 300 ºC.

Dislocations are created in two ways, those arising for statistical reasons and those arising from the geometry of the indenter. This increases the effective yield strength of the material which in turn means an increase in hardness. For the centre image, corresponding to the film with annealing at 180 °C, the tip rounding effect can be observed for an indentation depth of 7 to 20 nm as there is a clear drop in hardness. As the

penetration depth increases, the signal of the film starts to overlap the signal of the substrate. This is expected since the penetration depth is higher than the film thickness and, therefore, the properties being probed correspond to the ones of the substrate. In Figure 3.2, the same nanoindentation measurements are presented for the Mo sample with a thickness of 180 nm, where the tip rounding effect is also present.

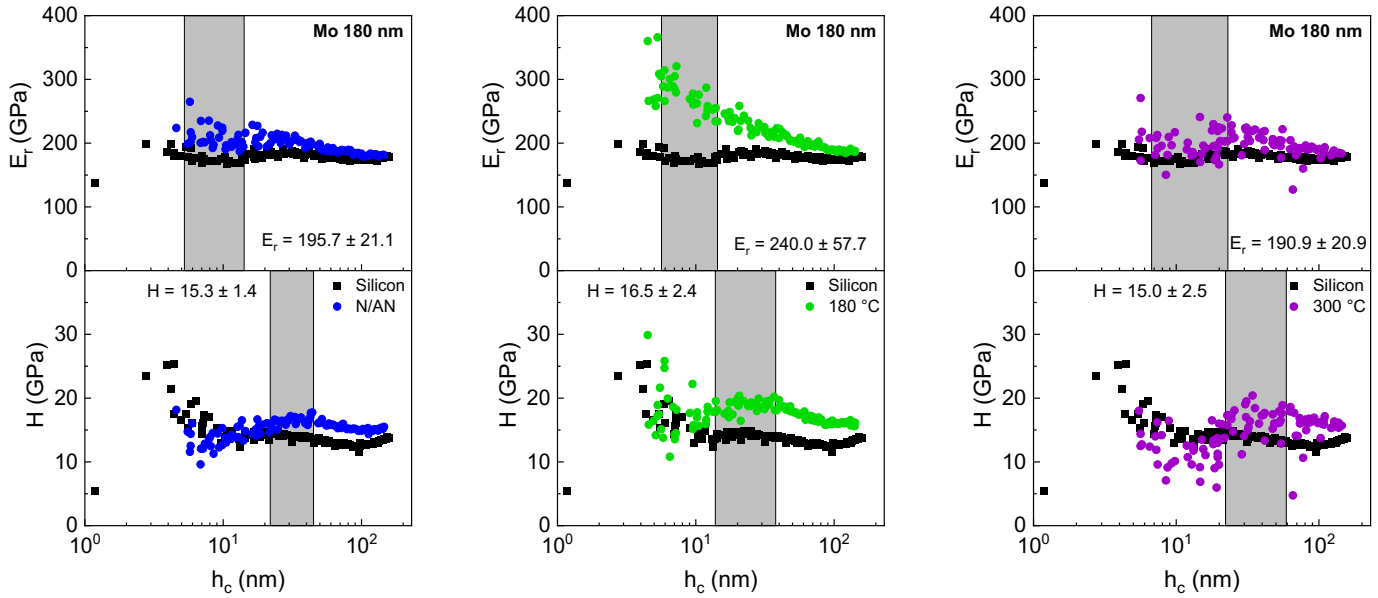

Figure 3.2 — Nanoindentation measurements for Young's modulus and hardness for Mo with a thickness of 180 nm: (left) as deposited; (centre) annealed at 180 ºC; (right) annealed at 300 ºC.

Figure 3.3 also presents the graphics obtained from the indentation measurements for the Mo sample with a thickness of 439 nm. For the right image, corresponding to the sample annealed at 300 ºC, it is observed a clear dispersion of values for both Young's modulus and hardness measurement. For this reason, further investigation was performed on this specific sample to better understand firstly, the surface morphology and secondly, the composition of the film.

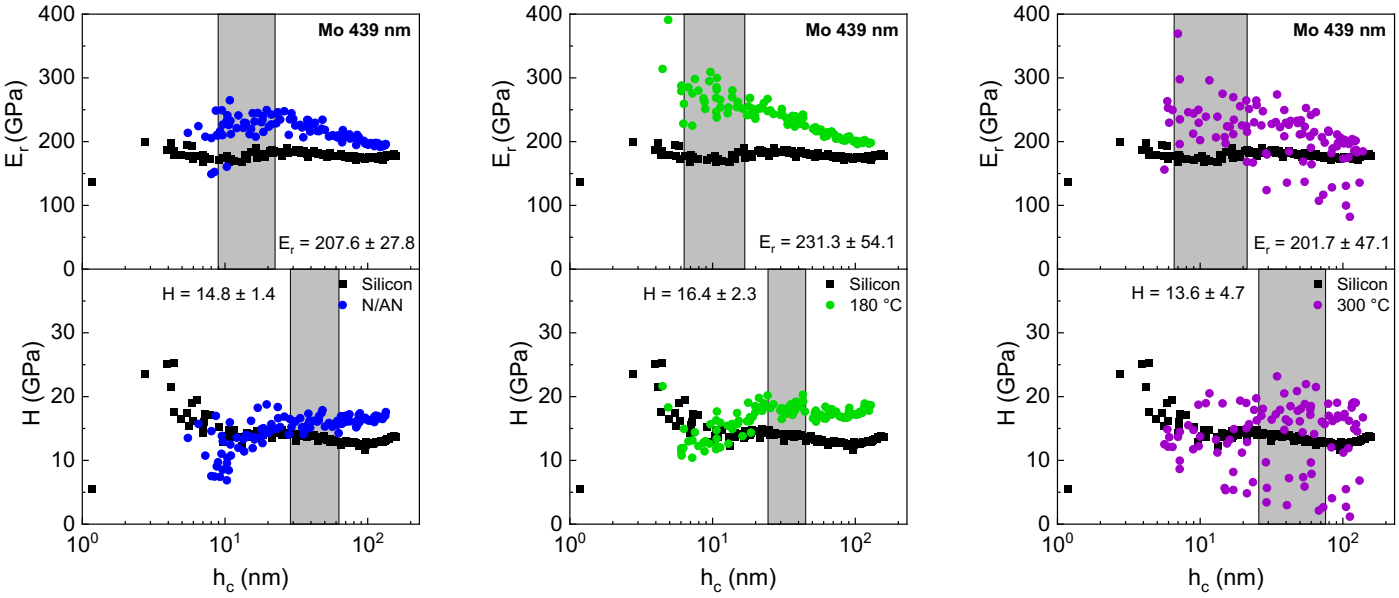

Figure 3.3 — Nanoindentation measurements for Young's modulus and hardness for Mo with a thickness of 439 nm: (left) as deposited; (centre) annealed at 180 ºC; (right) annealed at 300 ºC.

A pre-test Scanning Probe Microscopy (SPM) imaging of the testing site enables the direct measurement of the surface morphology (e.g., microstructure, topography, roughness) with nanometer resolution and is critical for avoiding surface defects before testing. Because of this, the nanoindentation measurements present in this study are the ones performed a second time with a pre-test SPM imaging that is a feature of the nanoindenter *TI 950*. For comparison proposes, Figure 3.4 represents the SPM images of topography (top) and lateral force images (bottom) for the Mo sample with a thickness of 93 nm with respective annealing conditions. For the films as deposited (left) and with annealing of 180 ºC (centre), the films are considered conformable with a nearly constant thickness on both horizontal and vertical surfaces. Nonetheless, for the film with annealing at 300 ºC (right), two distinct observations can be made. Firstly, the film exhibits a polycrystalline microstructure with random crystallographic grain orientations. And secondly, some structural alterations can be observed with also an increase of surface roughness. In Figure 3.5 it is shown the corresponding SPM images for the Mo film with a thickness of 439 nm. The films as deposited (left) and with annealing of 180 ºC (centre) are also considered conformable but a substantial alteration in the structure and morphology of the film with annealing at 300 ºC (left) is observed in addition to a considerable increase in the surface roughness.

SPM imaging for Mo with a thickness of 93 nm

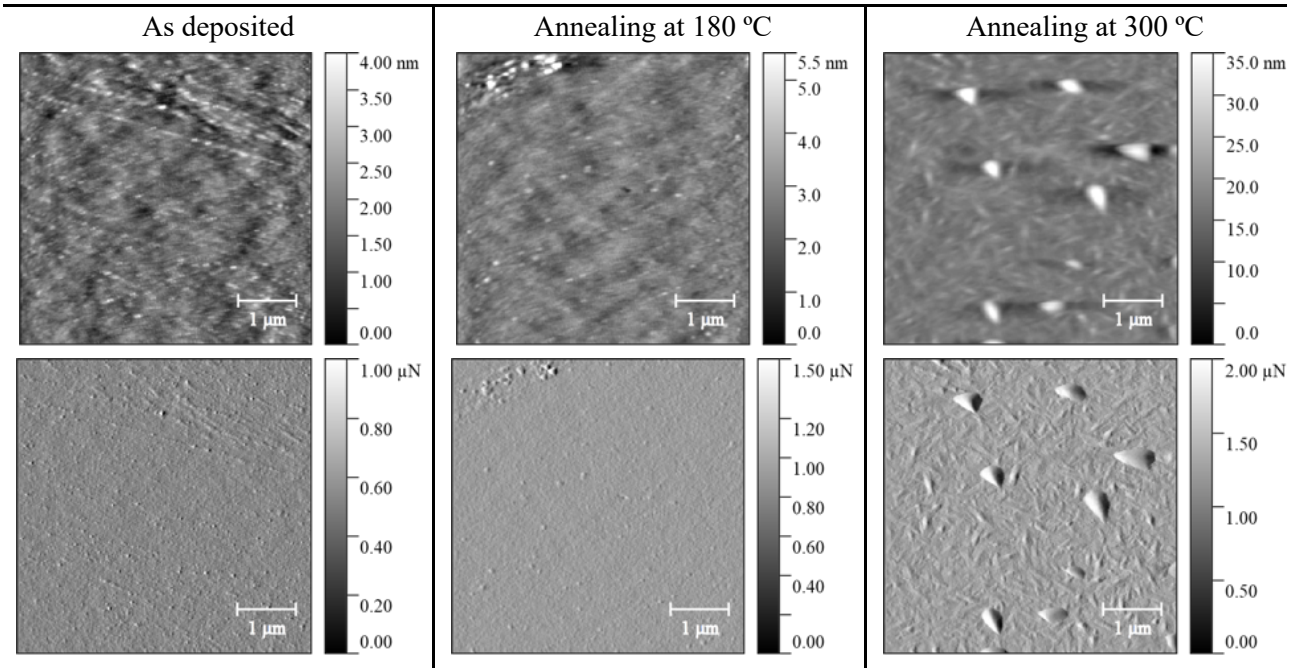

Figure 3.4 — In-situ SPM imaging for Mo with a thickness of 93 nm, (top) topography image, (bottom) lateral force imaging: (left) as deposited; (centre) annealed at 180 ºC; (right) annealed at 300 ºC.

For this reason, further studies were conducted to determine the composition of the film by resorting to Energy-Dispersive X-ray Spectroscopy (EDS) technique. This technique allowed for the elemental analysis of the Mo sample with a thickness of 439 nm annealed at 300 ºC and the obtained spectra is presented in Figure 3.6. The presence of both Mo and Si is anticipated because the molybdenum was deposited in a silicon substrate. Because no chemical elements were detected other than the expected ones, the hypothesis of contamination was ruled out. However, further conclusions can be drawn from the elemental mapping of the sample in question (Appendix B.2, Figure B.2.1), where it is shown that the composition of the irregularities has oxygen. Hence, the formation of molybdenum oxide is the cause of this phenomenon. This is attributed to the fact that the annealing process was open air.

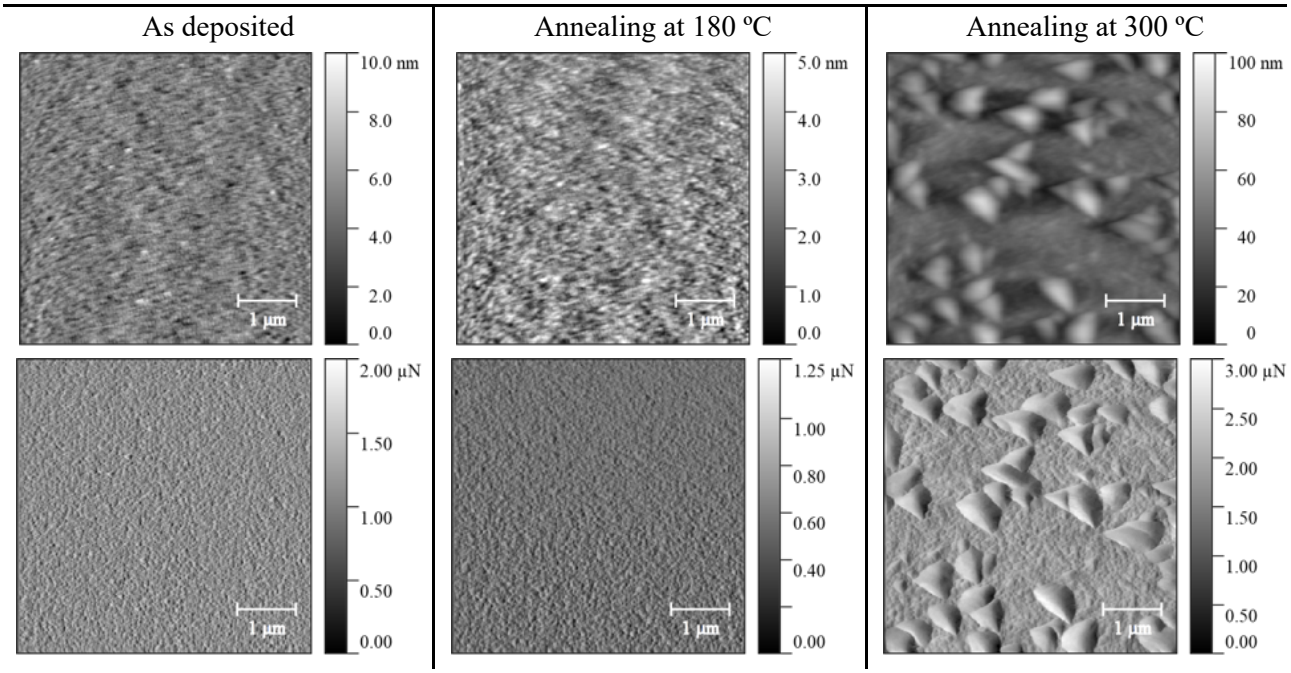

Figure 3.5 — In-situ SPM imaging for Mo with a thickness of 439 nm, (top) topography image, (bottom) lateral force imaging: (left) as deposited; (centre) annealed at 180 ºC; (right) annealed at 300 ºC.

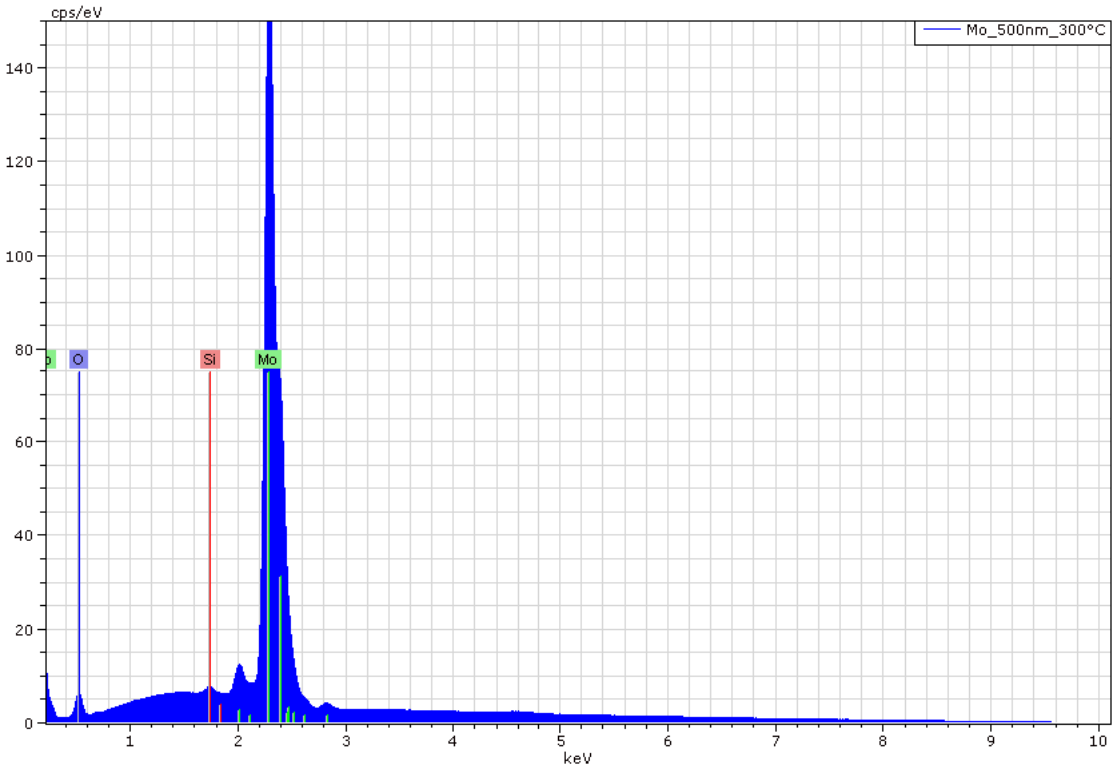

Figure 3.6 — Energy dispersive X-ray (EDS) spectra of Mo with a thickness of 439 nm annealed at 300 ºC.

Regarding the mechanical properties of the IGZO thin films, Figure 3.7 shows the nanoindentation measurements for a film thickness of 135 nm with the respective annealing conditions. The tip-rounding effect is present in all graphics. Given the film thickness, it would be expected, in similarity to the Mo thin films measurement, to observe, as the contact depth increases, a tendency towards the substrate values for both Young's modulus and hardness due to the substrate influence. However, this is not the case for the

nanoindentation measurements for all IGZO films and this is not fully understood as the measurements were repeated and the same occurred. Potential reasons for this behaviour can be strongly material-dependent interactions between tip and film or high intrinsic film stress. Figure B.3.1 and Figure B.3.2 in Appendix B.3 show the nanoindentation measurements for IGZO films with a thickness of 261 nm for a thickness of 609 nm, respectively.

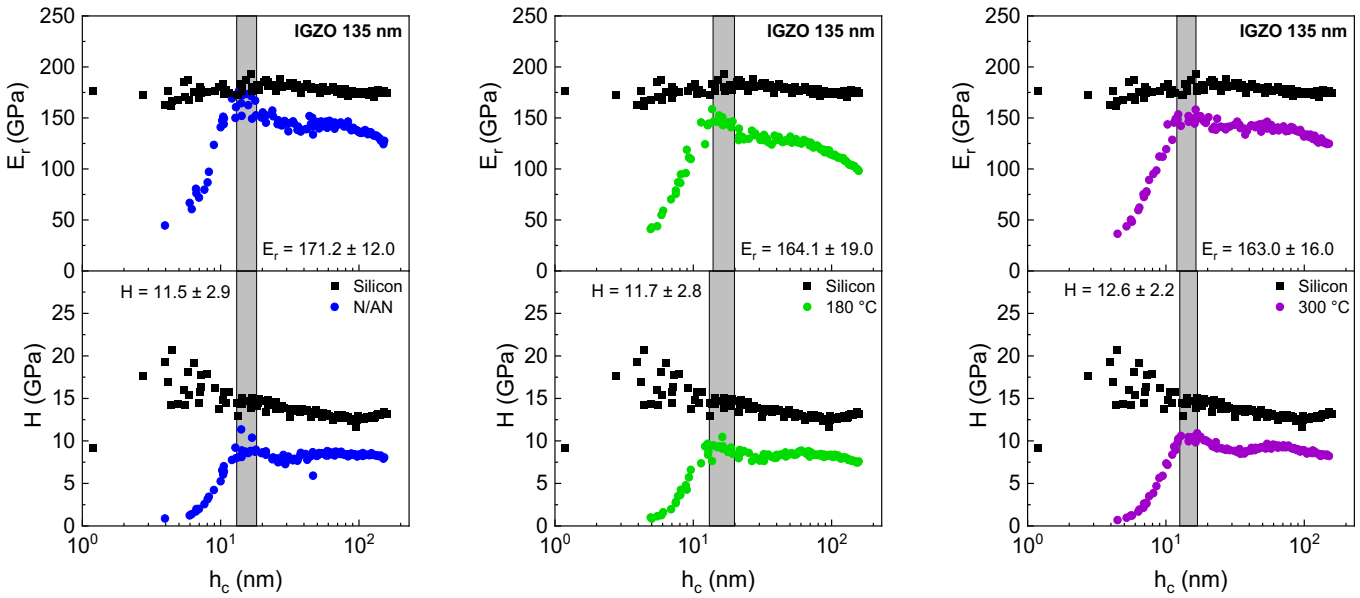

Figure 3.7 — Nanoindentation measurements for Young's modulus and hardness for IGZO with a thickness of 135 nm: (left) as deposited; (centre) annealed at 180 ºC; (right) annealed at 300 ºC.

Table 3.2 summarizes the mechanical properties of the Mo and IGZO thin films, obtained using the nanoindentation technique. Young's modulus is an indirect measurement, and it is calculated from the reduced Young's modulus and Poisson's ratio by $E = E_r(1 - \nu^2)$. Poisson's values were obtained from the literature, with 0.31[89] for molybdenum and 0.36[90] for IGZO.

For Mo, films with annealing at 180 ºC exhibit better mechanical properties given the higher values for Young's modulus and hardness. This means that these films are less prone to deformation for the same amount of stress and more resistant to localized plastic deformation. Even though this is not the case for the film with a smaller thickness (93 nm), it is important to point out that the nanoindentation measurements for a thickness this small are extremely challenging and cannot be entirely trustworthy, therefore, the previous conclusions are still valid. However, the obtained values for Young's modulus show considerable differences concerning the Mo literature bulk value of 324 GPa.[91] But this is expected as previously mentioned in Chapter 1.2, given the low thicknesses of the studied films. This does not pose a problem as, for a bendable device, high values for both Young's modulus and hardness would compromise flexibility. One other aspect that should be taken into consideration is the dispersion of values. Despite higher values for the standard deviation of the films annealed at 180 ºC, the data visualization of the nanoindentation measurements is very important, as the values follow an overall tendency, while for the samples annealed at 300 ºC, the values are extremely scattered. The Mo thin films with annealing at 300 ºC, exhibit poor mechanical properties due to the inferior quality of the films that translates into a high surface roughness. For a multilayer system, as in the case of the TFTs fabricated at *CENIMAT-i3N*, this will inevitably compromise the overall mechanical properties of the device.

In the case of the IGZO thin films, no tendency for Young's modulus and hardness is observed with the annealing process. This means that the mechanical properties of the IGZO thin films are not influenced by the

temperature processes relevant to this study. Therefore, when designing more mechanically robust devices with IGZO thin films, the annealing process must take into consideration implications on other properties other than the mechanical ones.

Table 3.2 — Mechanical properties of Mo and IGZO thin films for respective thicknesses and annealing conditions obtained from nanoindentation.

Sample	Thickness (nm)	Annealing condition	Poisson's ratio	Reduced Young's modulus (GPa)	Young's modulus (GPa)	Hardness (GPa)
Mo	93	No annealing	0.31	222.4 ± 13.8	201.0 ± 12.5	16.1 ± 2.2
		180 ºC		194.0 ± 17.7	175.4 ± 16.0	15.2 ± 1.3
		300 ºC		189.5 ± 20.1	171.3 ± 18.2	15.1 ± 1.4
	180	No annealing		195.7 ± 21.1	176.9 ± 19.1	15.3 ± 1.4
		180 ºC		240.0 ± 57.7	216.9 ± 52.1	16.5 ± 2.4
		300 ºC		190.9 ± 20.9	172.5 ± 18.9	15.0 ± 2.5
	439	No annealing		207. 6 ± 27.8	187.6 ± 25.1	14.8 ± 1.4
		180 ºC		231.3 ± 54.1	209.1 ± 48.9	16.4 ± 2.3
		300 ºC		201.7 ± 47.1	182.3 ± 42.6	13.6 ± 4.7
IGZO	135	No annealing	0.36	171.2 ± 12.0	149.0 ± 10.4	11.5 ± 2.9
		180 ºC		164.1 ± 19.0	142.8 ± 16.5	11.7 ± 2.8
		300 ºC		163.0 ± 16.0	141.9 ± 13.9	12.6 ± 2.2
	261	No annealing		157.2 ± 26.0	136.8 ± 22.6	10.7 ± 3.3
		180 ºC		159.7 ± 22.9	139.0 ± 19.9	11.4 ± 3.1
		300 ºC		162.4 ± 23.5	141.3 ± 20.4	11.7 ± 2.9
	609	No annealing		149.3 ± 32.9	129.9 ± 28.6	10.3 ± 3.5
		180 ºC		155.2 ± 27.7	135.1 ± 24.1	11.0 ± 3.1
		300 ºC		148.6 ± 35.4	129.3 ± 30.8	10.6 ± 3.4

3.2.2 Ta_2O_5 and Multilayer Stack Thin Films

Figure B.4.1 and Figure B.4.2 in Appendix B.4 correspond to the nanoindentation measurements performed for the Ta_2O_5 films with a thickness of 312 nm, and the multilayer stack (Ta_2O_5/SiO_2) with a thickness of 343 nm, respectively. All measurements exhibit tip-rounding effect for the initial penetration depths and the substrate influence is not pronounced due to the film's thicknesses. Table 3.3 displays the mechanical properties obtained from the data analysis for both the Ta_2O_5 and the multilayer stack thin films. Since the SiO_2 layer, from the perspective of a nanoindentation measurement, is extremely thin (31 nm), the content of its value is hard to reach. Hence, this layer's influence on the properties can be measurable, but it cannot be individually characterized. A Poisson's ratio value of 0.27[92] for Ta_2O_5 was obtained from the literature. In the case of the multilayer, the Poisson's value can be assumed as the same due to the SiO_2 small layer thickness. For the Ta_2O_5 sample, Young's modulus values are in accordance with the literature values for this thin film that ranges from

130 to 150 GPa.[75] The obtained hardness is slightly higher than the literature values (9 to 10 GPa).[75] Even though Young's modulus values of SiO_2 published in the literature are widely scattered,[93] these are all smaller than Young's modulus values for Ta_2O_5. Hence, the multilayer thin film exhibits a lower Young's modulus than the single Ta_2O_5 layer. No direct conclusion can be made for the annealing influence on the mechanical properties of the films, as there is only one thickness being studied for each sample.

Table 3.3 — Mechanical properties of Ta_2O_5 and Ta_2O_5/SiO_2 thin films for respective thickness and annealing conditions obtained from nanoindentation.

Sample	Thickness (nm)	Annealing condition	Poisson's ratio	Reduced Young's modulus (GPa)	Young's modulus (GPa)	Hardness (GPa)
Ta_2O_5	312	No annealing	0.27	158.7 ± 24.9	147.1 ± 23.1	10.6 ± 3.7
		180 ºC		160.2 ± 25.5	148.5 ± 23.6	10.5 ± 3.7
		300 ºC		151.1 ± 32.8	140.1 ± 30.4	10.5 ± 3.7
Ta_2O_5/SiO_2	343	No annealing	0.27	145.7 ± 36.5	134.8 ± 33.8	10.4 ± 3.7
		180 ºC		141.6 ± 37.3	131.3 ± 34.6	10.4 ± 3.7
		300 ºC		149.9 ± 35.4	139.0 ± 32.8	10.7 ± 3.4

3.2.3 Polyimide Thin Films

Quasi-static measurements were also performed on polyimide thin films to acquire Young's modulus for each sample, and to give a pre-characterization before the viscoelastic properties of these samples. Figure 3.8 presents the nanoindentation measurements for the PI with the highest thickness of the study when annealed at 250 ºC (green on the left) and at 350 ºC (pink on the right). Because polymers possess weaker intermolecular interactions[78] when compared to metals and ceramics, Young's modulus is smaller. Figure B.5.1 and Figure B.5.2 in Appendix B.5 show the quasi-static nanoindentation measurements for PI films. The values obtained from the quasi-static nanoindentation measurements of all the PI samples are in Table 3.4. The Poisson's ratio value was assumed 0.34. For the highest annealing temperature, there is a tendency for higher Young's modulus values. In fact, annealing is a popular post-process whose main goal is to enhance the mechanical strength and increase the percentage of crystallinity of the material. It involves gently reheating the material to its glass transition temperature or just above, but below its melting temperature, holding it there for a specified time and then slowly allowing it to cool. This reheating and extended cooling increases the amount of large crystalline structures in the polymer and redistributes the stresses within the printed part leading to higher crystallinity, strength, and stiffness.[79, 80] Because the annealing temperature of 350 ºC is closer to the glass transition temperature (360 ºC for PI 2610), it reveals the higher Young's modulus values.

As the viscoelastic material parameters determined using the nano-DMA technique resemble better the mechanical behaviour of the PI, those should be used later in FE modelling. The linear elastic values derived here from the quasi-static measurements only give a first hint of the overall stiffness of the studied PI.

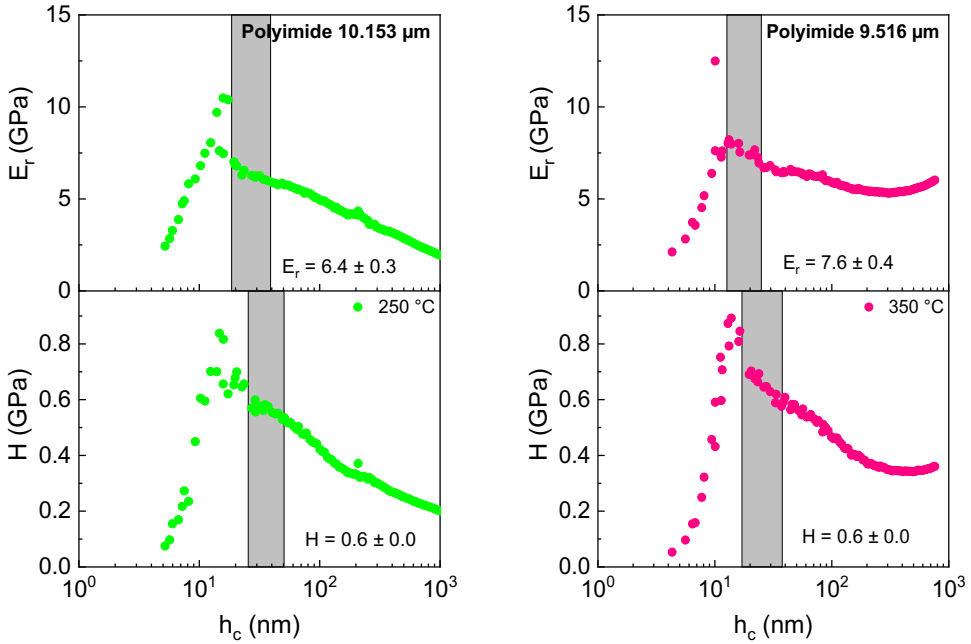

Figure 3.8 — Nanoindentation measurements for Young's modulus and hardness for PI with a thickness of: (left) 10.153 µm annealed at 250 ºC; (right) 9.516 µm annealed at 300 ºC.

Table 3.4 — Mechanical properties of PI thin films for respective thicknesses and annealing conditions obtained from nanoindentation.

Sample	Thickness (nm)	Annealing temperature (ºC)	Poisson's ratio	Reduced Young's modulus (GPa)	Young's modulus (GPa)	Hardness (GPa)
Polyimide	1.100	250	0.34	7.5 ± 0.4	6.6 ± 0.3	0.7 ± 0.1
	1.066	350		7.9 ± 0.4	7.0 ± 0.3	0.7 ± 0.1
	1.583	250		8.1 ± 0.2	7.2 ± 0.2	1.0 ± 0.1
	1.563	350		9.8 ± 1.6	8.7 ± 1.4	1.2 ± 0.1
	10.153	250		6.4 ± 0.3	5.7 ± 0.3	0.6 ± 0.0
	9.516	350		7.6 ± 0.4	6.7 ± 0.3	0.6 ± 0.0

3.3 Polyimide Viscoelastic Measurements with nano-Dynamic Mechanical Analysis

Because polymers show viscoelastic behaviour, it is important to experimentally assess these properties that characterize such behaviour. This section presents the results obtained from the nano-DMA technique, namely storage modulus, loss modulus and phase angle (tan δ). To achieve a complete picture of the dynamical mechanical behaviour of a polymer, the measurements were performed over a wide range of frequencies and temperatures, and it is possible to relate data obtained through a procedure known as time-temperature superposition, which is valid for thermorheologically simple materials (TSM). This is because the time and temperature dependence of the viscoelastic properties of polymers can be interrelated. For instance, a polymer that shows rubbery characteristics under a given set of testing conditions can be induced to display glassy behaviour by either increasing the frequency, testing time, or reducing the temperature. Frequencies lower than one Hertz require very slow ramp rates and for that reason not considered for this study. However, it is still important to

estimate behaviour at times that are inconvenient or impossible to measure experimentally. This can be done by the development of the master curve using time-temperature superposition which is a collection of frequency- and temperature-dependent data that have been treated so they are displayed as one curve against an axis of shifted values. Usually, this is done using a frequency scale for the x-axis and temperature as the variable to create the curves. Hence, the data can be superpositioned to generate one curve. The model used for the shift is the Williams-Landel-Ferry (WLF), where the shift factor is given as:

$$\log a_T = \frac{-C_1(T-T_r)}{C_2+(T-T_r)} \tag{3.1}$$

Where a_T is the shift factor, C_1 and C_2 are material constants, T is the temperature, and T_r is the reference temperature. Because this model is applied directly in the ANSYS environment, this study focuses mainly on the obtention of the input data.

3.3.1 Storage Modulus

As previously mentioned in Chapter 1.2.2, the storage modulus is a measure of the energy stored and recovered per cycle and is defined as the stress in phase with the strain in a sinusoidal shear deformation divided by the strain. The storage modulus can be understood as the linear elastic part of the viscoelastic material behaviour to the complex modulus. The nano-DMA measurements of storage modulus in relation to the test frequency at different temperatures are shown in Figure 3.9 for the PI thin film with a thickness of 9.516 µm annealed at 350 ºC. However, from these results, it is already possible to affirm that some problems took place with the experimental part of these measurements. For higher temperatures towards the glass transition temperature, the storage modulus should normally decrease, and although that is here only the case for the temperature of 141.8 ºC, it is not transversal to the overall tendency of the data. As polymers heat, they normally display more viscous behaviour, which is accompanied by an increase in the loss modulus, see below.

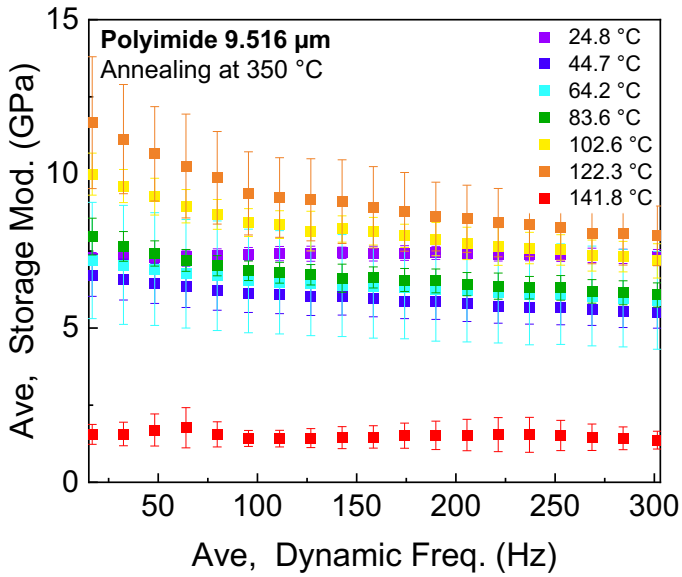

Figure 3.9 — Nano-DMA measurements of storage modulus vs frequency at different temperatures for PI with a thickness of 9.516 µm annealed at 350 ºC.

Figures B.6.1-3 in Appendix B.6 show the nano-DMA measurements of storage modulus over frequency for PI films annealed at 250 ºC with a thickness of 1.100, 1.583, 10.153 µm, respectively. Figures B.6.4-5 in

Appendix B.6 show the nano-DMA measurements for PI films annealed at 350 ºC with a thickness of 1.066 and 1.563 µm, respectively.

3.3.2 Loss Modulus

Loss modulus is a measure of the elastic energy dissipated or lost as heat per cycle of sinusoidal deformation and is defined as the stress 90º out of phase with the strain divided by the strain. It can be seen as the viscous, load rate-dependent part of the complex modulus. Its value should be lower for higher frequencies, because, on a molecular basis, the shorter the period of deformation, the lower is going to be the capacity for molecular or atomic adjustments capable of dissipating energy. Regarding the temperature influence on the loss modulus, it should increase until it reaches the glass transition temperature of the sample and starts to decrease for higher temperatures. However, the glass transition temperature was not achieved with these measurements. This would require a different experimental setup that would allow performing the measurements at higher temperatures given that the glass transition temperature is indicated as 360 ºC in the PI 2610 product bulletin. What also can be seen in the loss modulus data is that its values are much smaller compared to the storage modulus, Figure 3.10. This means the PI studied here has no pronounced viscoelastic character.

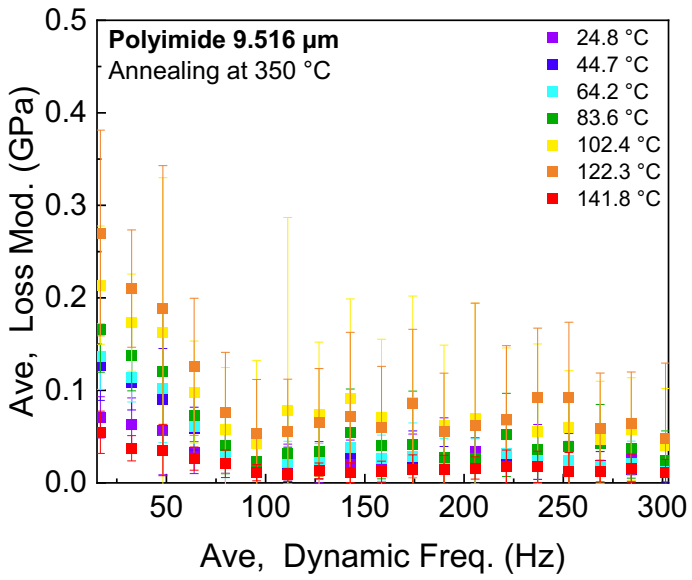

Figure 3.10 — Nano-DMA measurements of loss modulus vs frequency at different temperatures for PI with a thickness of 9.516 µm annealed at 350 ºC.

Figures B.7.1-3 in Appendix B.7 show the nano-DMA measurements of loss modulus over frequency for PI films annealed at 250 ºC with a thickness of 1.100, 1.583, 10.153 µm, respectively. Figures B.7.4-5 in Appendix B.7 show the nano-DMA measurements for PI films annealed at 350 ºC with a thickness of 1.066 and 1.563 µm, respectively.

3.3.3 Tan δ

The tangent of the phase angle is a property also known as damping or loss tangent and is an indicator of how efficiently the material loses energy to molecular rearrangements and internal friction. It is a relative measure of the viscous and elastic properties of a material. The height and area under the tan δ curve give an indicator of the total amount of energy that can be absorbed by the material. A larger area under the tan curve indicates

greater molecular mobility, which translated into higher inner material damping, meaning that the material can better absorb and dissipate energy. This is critical for the case of this study since we intend to design more mechanically robust devices. Tan δ also varies with temperature and frequency. The phase angle in relation to the test frequency at different temperatures is shown in Figure 3.11 for the PI thin film with a thickness of 9.516 µm annealed at 350 ºC.

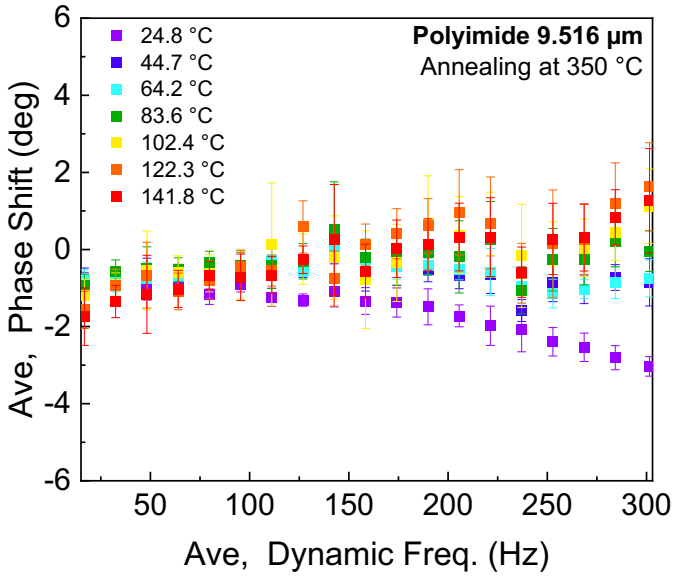

Figure 3.11 — Nano-DMA measurements of tan δ vs frequency at different temperatures for PI with a thickness of 9.516 µm annealed at 350 ºC.

Figures B.8.1-3 in Appendix B.8 show the nano-DMA measurements of phase angle over frequency for PI films annealed at 250 ºC with a thickness of 1.100, 1.583, 10.153 µm, respectively. Figures B.8.4-5 in Appendix B.8 show the nano-DMA measurements for PI films annealed at 350 ºC with a thickness of 1.066 and 1.563 µm, respectively.

3.4 FEM Simulations with ANSYS

The FE simulations were done for the objective of this work, namely, to transfer the experimental determined nanomechanical data to FE material models as well as a simple proof-of-concept for an upon-based FEM workflow, are chosen to be simple. The defined geometry is the same for all specimens, and for the objectives of this work, a simple cube with 50 µm of edge dimension was the choice of geometry. Posteriorly, the mesh is established, and boundary conditions are then defined (a displacement of the top plane applied on the cubes as load BC as well as fixed support at the bottom of the cubes). The FEM loading scenario was applying loading in 1 s to 1 µm displacement of the top plane, 1 s hold, and 1 s unload. The viscoelastic reaction was also studied at 50% of the 1 µm displacement unload of the top surface. See Figure 3.14. The displacement values are negative due to the direction of the load vector (compressive), Figure 3.12.

Due to time constraints attributed to the challenging experimental work, the FEM simulations were performed for a selected group of samples. Because this study compromises two different types of material behaviour, it was fundamental to choose materials that obey different material models. Mo and IGZO were chosen for the application of the linear elastic model, and PI for the viscoelastic model, as it is the only viscoelastic material in this study. The films with the smaller thicknesses were selected, in the case of the Mo and

IGZO for the simulation because, in a TFT stack, these material layers are in the order of a few nanometres. Hence, for coherence with the motivation for this study, the thinner film's properties are of greater relevance. However, it is important to note that nanoindentation measurements for these films are very challenging, and the data obtained from them can pose some validity questions. For both Mo and IGZO, two samples with distinct annealing conditions were chosen. Because the Mo thin films exhibited better mechanical properties for annealing at 180 ºC, even if not the case for this specific thickness, the respective sample was chosen for this simulation. As for the polyimide, the sample with a thickness of 9.516 µm annealed at 350 ºC was chosen for both a linear elastic model and a viscoelastic model simulation.

To characterize the films, Young's modulus obtained from the quasi-static measurements as well as other material properties were introduced in the ANSYS workspace. Table 3.5 summarizes the properties defined in ANSYS for the respective thin films. For the modelling of the viscoelasticity, the temperature- and frequency-dependent modulus data were fed into the ANSYS workplace, and the material model was internally parameterized using a fit of the experimental data with a Prony series for shear relaxation

Table 3.5 — Material properties defined in ANSYS for the selected Mo, IGZO and PI thin films.

	Thickness	**Annealing conditions**	**Poisson's ratio**	**Young's modulus (GPa)**
Mo	93 nm	No annealing	0.31	201.0 ± 12.5
		180 ºC		175.4 ± 16.0
IGZO	135 nm	No annealing	0.36	149.0 ± 10.4
		300 ºC		141.9 ± 13.9
PI	9.516 µm	350 ºC	0.34	6.7 ± 0.3

Because the materials have different Young's modulus, for the same load, different deformations can be observed. For Mo, because it is a material with a higher Young's modulus, the deformation is less significant, hence the lower deformation value. For the PI viscoelastic material model, the simulation results show a clear viscoelastic behaviour as the material shows a significant deformation when compared to linear elastic materials.

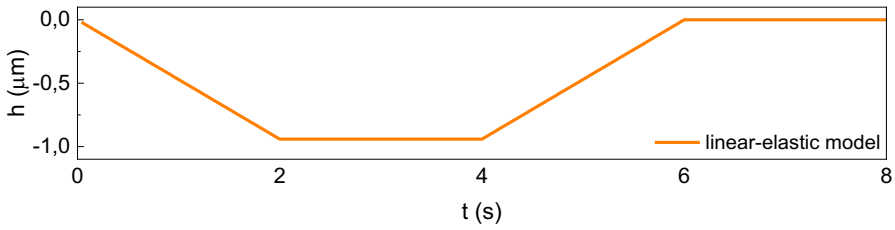

Figure 3.12 — Graphic of the boundary condition of the sample PI for displacement over time obtained in ANSYS for linear-elastic behaviour.

Figure 3.15 displays the simulation results for equivalent stress 1 s after unloading 50% of 1 µm displacement of the top surface, and Figure 3.13 shows the graphic of the reaction stresses of the two material models for the PI sample where it can be observed the difference between linear elasticity and viscoelasticity. Equivalent stress allows the view of the stress of the structure in one plot and is an essential tool in engineering as can be used to determine the ductility of a material. By Newton's laws of motion, any external forces being applied to a structure in macroscopic static equilibrium must be balanced by internal reaction forces. Stress

empresses these internal forces that neighbouring particles exert on each other. Because metals like Mo exhibit strong bonds between atoms, the stronger is going to be the internal reaction of the overall structure that contradicts the applied load. Hence a higher stress value for the Mo material model. As for a viscoelastic material, the bonds between atoms are weaker and there will not exert as many internal forces on each other in reaction to the load. This translates into a lower stress value and a higher material ductility. However, polyimide's stress values did not work in the viscoelastic model as the obtained stress value is practically zero. This is due to the strange raw data results that were obtained from the nano-DMA measurements. The nano-DMA experimental work must be redone to acquire relevant results.

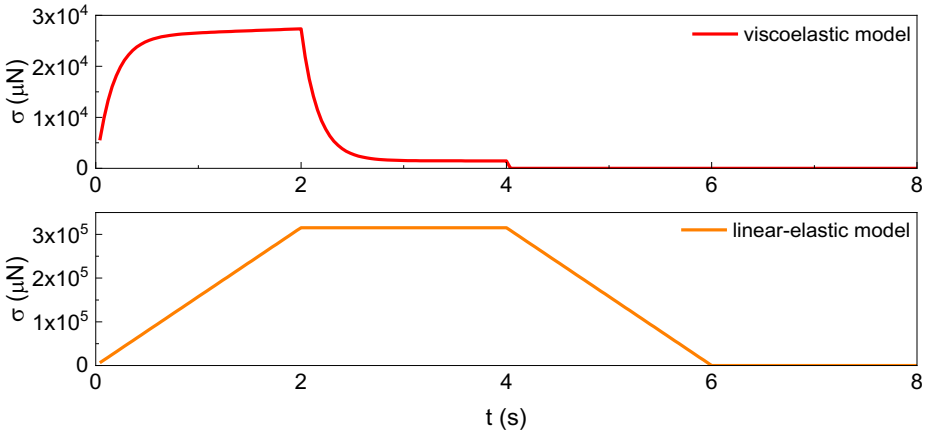

Figure 3.13 — Graphic of the PI sample boundary condition of relative stress over time obtained in ANSYS for: (top) viscoelastic model; (bottom) linear elastic model.

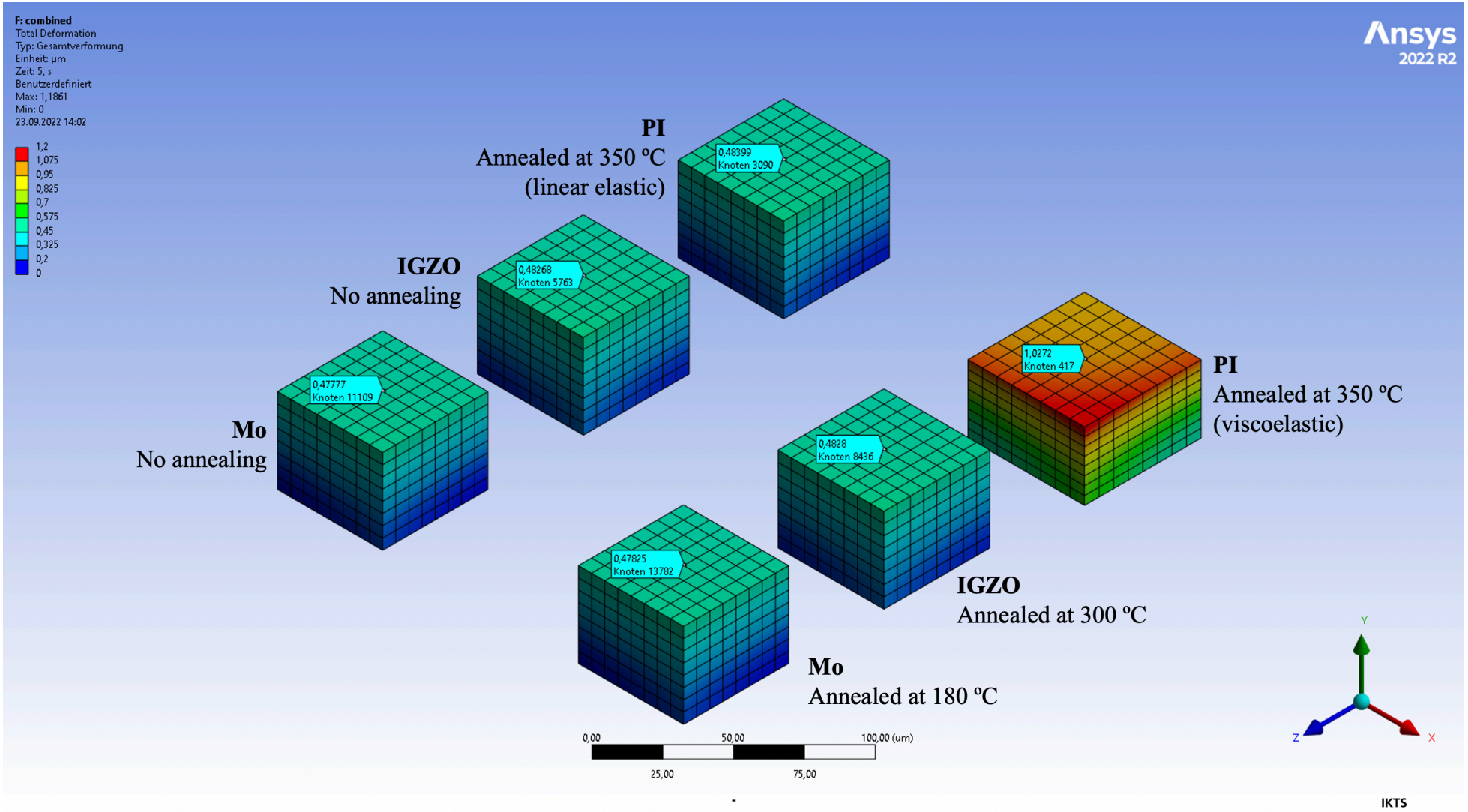

Figure 3.14 — FEM simulation results (1 s after unloading 50% of 1 µm displacement of the top surface) using ANSYS showing the displacement over time for the linear elastic model (Mo, IGZO and PI) and for the viscoelastic model (PI).

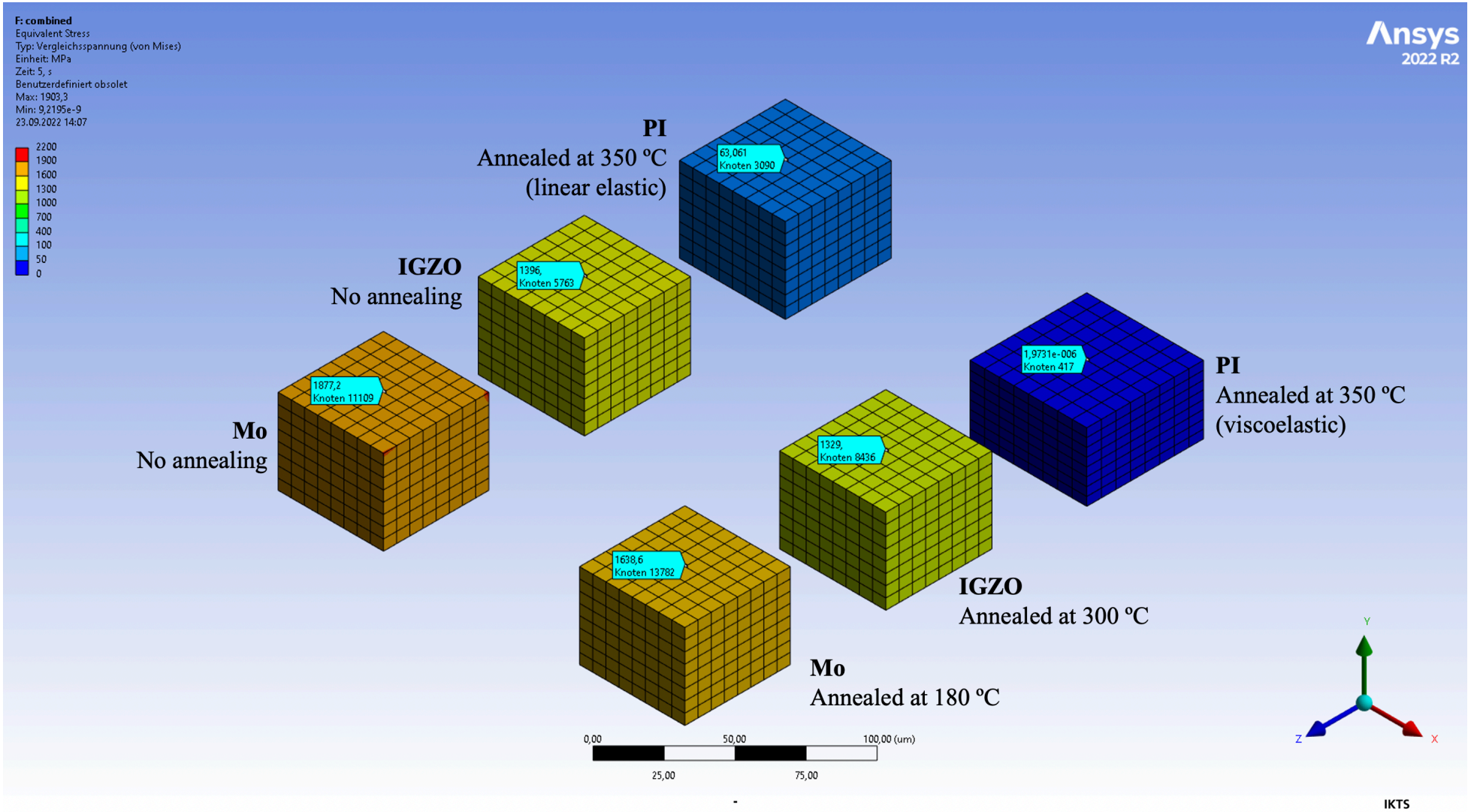

Figure 3.15 — FEM simulation results 1 s after unloading 50% of 1 µm displacement of the top surface) using ANSYS showing the equivalent stress over time for the linear elastic model (Mo, IGZO and PI) and for the viscoelastic model (PI).

4

CONCLUSIONS AND FUTURE PERSPECTIVES

This work not only proves that the concept of simulating TFTs in FEM is possible but presents the workflow that should be adopted when doing so.

For thin films that exhibit linear elastic behaviour in the elastic regime, such as metals (Mo), semiconductors (IGZO) and dielectrics (Ta_2O_5 and Ta_2O_5/SiO_2), quasi-static nanoindentation was the adopted technique to determine the mechanical properties of the films (Young's modulus). As for polymeric thin films (PI), they exhibit viscoelastic behaviour in the elastic regime and the nanoscale Dynamic Mechanical Analysis technique allowed for the extraction of the viscoelastic material properties (storage modulus, loss modulus and tan δ). With the data obtained from the challenging measurements, a linear elastic material model (Mo, IGZO, Ta_2O_5 and Ta_2O_5/SiO_2) and a viscoelastic material model (PI) were parametrized, a geometry was defined, meshed, boundary conditions were set, and the FEM solutions of the continuum mechanics problem were achieved. Hereby, proving the concept of this study.

In the data obtained from the nanoindentation quasi-static measurements, the following conclusions were obtained:

- The Mo thin films annealed at 180 ºC exhibit the best mechanical properties (higher Young's modulus).
- Annealing at 300 ºC is critical for the mechanical properties of the Mo thin films. Thus, when it comes to the process of designing a TFT for flexible electronics applications, this thermal process temperature should not be considered as it would pose serious implications on the mechanical aspect of a multilayer/TFT stack.
- Annealing of IGZO thin films has no impact on their mechanical properties.
- Further quasi-static nanoindentation measurements should be performed for Ta_2O_5 and Ta_2O_5/SiO_2 thin films with different thicknesses for each, to assess the influence of the annealing process on the mechanical properties of these films.

However, it is very important to consider that, although in this study the films were characterized individually, a TFT device is composed of multilayers of these films. Therefore, other studies, in terms of mechanical behaviour, must be considered for multilayer stacks, such as, for instance, the evaluation of interfacial strength of the thin film multilayer.

The experimental data obtained for the nano-DMA measurement had some experimental peculiarities and should be considered as not very exact. Thus, to obtain a valid viscoelastic material model, the nano-DMA analysis would have to be repeated, ideally, with a setup with higher thermal stability. For temperature measurements, there are commercially available systems that possess many advantages that could significantly reduce measurement errors. These allow for reaching higher temperature values (600 ºC) and achieving high thermal stability and short stabilization times. Another aspect, and that these commercial systems consider, is the temperature difference between the tip and the specimen, as it can create thermal drift and, consequentially, errors in the measurement.

The next step to complement this study is not only to acquire a bigger database of the mechanical properties of other thin film materials used in oxide TFTs, but also to improve the complexity of the simulations, and, consequentially, achieve a detailed simulation of TFTs in FEM. This can be done with a bigger variety of continuum mechanics problems, such as critical stress interface and thermal stress for instance and significantly improving the defined geometries until they are in accordance with the desired TFT structure.

REFERENCES

[1] Q. Cao *et al.,* "Medium-scale carbon nanotube thin-film integrated circuits on flexible plastic substrates," *Nature*, vol. 454, no. 7203, pp. 495–500, 2008, doi: 10.1038/nature07110.

[2] Y.-S. Li *et al.,* "Flexible Complementary Oxide–Semiconductor-Based Circuits Employing n-Channel ZnO and p-Channel SnO Thin-Film Transistors," *IEEE Electron Device Letters*, vol. 37, no. 1, pp. 46–49, 2016, doi: 10.1109/LED.2015.2501843.

[3] G. H. Gelinck *et al.,* "Flexible active-matrix displays and shift registers based on solution-processed organic transistors," *Nature Materials*, vol. 3, no. 2, pp. 106–110, 2004, doi: 10.1038/nmat1061.

[4] K. J. Allen, "Reel to Real: Prospects for Flexible Displays," *Proceedings of the IEEE*, vol. 93, no. 8, pp. 1394–1399, 2005, doi: 10.1109/JPROC.2005.851511.

[5] K. Bock, "Polymer Electronics Systems - Polytronics," *Proceedings of the IEEE*, vol. 93, no. 8, pp. 1400–1406, 2005, doi: 10.1109/JPROC.2005.851513.

[6] Jae Kyeong Jeong, "The status and perspectives of metal oxide thin-film transistors for active matrix flexible displays," *Semiconductor Science and Technology*, vol. 26, no. 3, p. 34008, 2011, doi: 10.1088/0268-1242/26/3/034008.

[7] P. Heremans, "Electronics on plastic foil, for applications in flexible OLED displays, sensor arrays and circuits," in *2014 21st International Workshop on Active-Matrix Flatpanel Displays and Devices (AM-FPD)*, 2014, pp. 1–4.

[8] H. Xu *et al.,* "A flexible AMOLED display on the PEN substrate driven by oxide thin-film transistors using anodized aluminium oxide as dielectric," *J. Mater. Chem. C*, vol. 2, no. 7, pp. 1255–1259, 2014, doi: 10.1039/C3TC31710B.

[9] John A. Rogers *et al.,* "Paper-like electronic displays: Large-area rubber-stamped plastic sheets of electronics and microencapsulated electrophoretic inks," *Proceedings of the National Academy of Sciences*, vol. 98, no. 9, pp. 4835–4840, 2001, doi: 10.1073/pnas.091588098.

[10] M. Ito, M. Kon, M. Ishizaki, and N. Sekine, "A flexible active-matrix TFT array with amorphous oxide semiconductors for electronic paper," *IDW/AD'05 - Proceedings of the 12th International Display Workshops in Conjunction with Asia Display 2005*, pp. 845–846, 2005.

[11] A. Nathan and B. R. Chalamala, "Special Issue on Flexible Electronics Technology, Part II: Materials and Devices," *Proceedings of the IEEE*, vol. 93, no. 8, pp. 1391–1393, 2005, doi: 10.1109/JPROC.2005.851509.

[12] X. Pu *et al.,* "A Self-Charging Power Unit by Integration of a Textile Triboelectric Nanogenerator and a Flexible Lithium-Ion Battery for Wearable Electronics," *Advanced Materials*, vol. 27, no. 15, pp. 2472–2478, 2015, doi: 10.1002/adma.201500311.

[13] Y. Khan *et al.,* "Flexible Hybrid Electronics: Direct Interfacing of Soft and Hard Electronics for Wearable Health Monitoring," *Advanced Functional Materials*, vol. 26, no. 47, pp. 8764–8775, 2016, doi: 10.1002/adfm.201603763.

[14] D.-H. Kim *et al.,* "Dissolvable films of silk fibroin for ultrathin conformal bio-integrated electronics," *Nature Materials*, vol. 9, no. 6, pp. 511–517, 2010, doi: 10.1038/nmat2745.

[15] A. K. Tripathi *et al.,* "Low-voltage gallium–indium–zinc–oxide thin film transistors based logic circuits on thin plastic foil: Building blocks for radio frequency identification application," *Appl. Phys. Lett.*, vol. 98, no. 16, p. 162102, 2011, doi: 10.1063/1.3579529.

[16] A. Nathan *et al.,* "Flexible Electronics: The Next Ubiquitous Platform," *Proceedings of the IEEE*, vol. 100, Special Centennial Issue, pp. 1486–1517, 2012, doi: 10.1109/JPROC.2012.2190168.

[17] N. Münzenrieder, L. Petti, C. Zysset, T. Kinkeldei, G. A. Salvatore, and G. Tröster, "Flexible Self-Aligned Amorphous InGaZnO Thin-Film Transistors With Submicrometer Channel Length and a Transit Frequency of 135 MHz," *IEEE Transactions on Electron Devices*, vol. 60, no. 9, pp. 2815–2820, 2013, doi: 10.1109/TED.2013.2274575.

[18] Y. Sun and J. A. Rogers, “Inorganic Semiconductors for Flexible Electronics,” *Advanced Materials*, vol. 19, no. 15, pp. 1897–1916, 2007, doi: 10.1002/adma.200602223.

[19] John A. Rogers, Takao Someya, and Yonggang Huang, “Materials and Mechanics for Stretchable Electronics,” *Science*, vol. 327, no. 5973, pp. 1603–1607, 2010, doi: 10.1126/science.1182383.

[20] T. Sekitani, M. Kaltenbrunner, T. Yokota, and T. Someya, “Imperceptible Electronic Skin,” *SID Symposium Digest of Technical Papers*, vol. 45, no. 1, pp. 122–125, 2014, doi: 10.1002/j.2168-0159.2014.tb00034.x.

[21] J. Neto, R. Chirila, A. S. Dahiya, A. Christou, D. Shakthivel, and R. Dahiya, “Skin-Inspired Thermoreceptors-Based Electronic Skin for Biomimicking Thermal Pain Reflexes,” *Advanced Science*, vol. 9, no. 27, p. 2201525, 2022, doi: 10.1002/advs.202201525.

[22] L. Petti *et al.,* “Influence of Mechanical Bending on Flexible InGaZnO-Based Ferroelectric Memory TFTs,” *IEEE Transactions on Electron Devices*, vol. 61, no. 4, pp. 1085–1092, 2014, doi: 10.1109/TED.2014.2304307.

[23] P. K. Weimer, “The TFT A New Thin-Film Transistor,” *Proceedings of the IRE*, vol. 50, no. 6, pp. 1462–1469, 1962, doi: 10.1109/JRPROC.1962.288190.

[24] J.-J. Huang *et al.,* “A 4.1-Inch Flexible QVGA AMOLED Using a Microcrystalline-Si:H TFT on a Polyimide Substrate,” *SID Symposium Digest of Technical Papers*, vol. 40, no. 1, pp. 866–869, 2009, doi: 10.1889/1.3256932.

[25] J.-K. Lee, Y.-S. Lim, C.-H. Park, Y.-I. Park, C.-D. Kim, and Y.-K. Hwang, “a-Si:H Thin-Film Transistor-Driven Flexible Color E-Paper Display on Flexible Substrates,” *IEEE Electron Device Letters*, vol. 31, no. 8, pp. 833–835, 2010, doi: 10.1109/LED.2010.2051531.

[26] C. D. Dimitrakopoulos and D. J. Mascaro, “Organic thin-film transistors: A review of recent advances,” *IBM Journal of Research and Development*, vol. 45, no. 1, pp. 11–27, 2001, doi: 10.1147/rd.451.0011.

[27] P. Lin and F. Yan, “Organic Thin-Film Transistors for Chemical and Biological Sensing,” *Advanced Materials*, vol. 24, no. 1, pp. 34–51, 2012, doi: 10.1002/adma.201103334.

[28] K. Nomura, H. Ohta, A. Takagi, T. Kamiya, M. Hirano, and H. Hosono, “Room-temperature fabrication of transparent flexible thin-film transistors using amorphous oxide semiconductors,” *Nature*, vol. 432, no. 7016, pp. 488–492, 2004, doi: 10.1038/nature03090.

[29] J.-Y. Kwon, D.-J. Lee, and K.-B. Kim, “Review paper: Transparent amorphous oxide semiconductor thin film transistor,” *Electronic Materials Letters*, vol. 7, no. 1, pp. 1–11, 2011, doi: 10.1007/s13391-011-0301-x.

[30] E. Fortunato, P. Barquinha, and R. Martins, “Oxide Semiconductor Thin-Film Transistors: A Review of Recent Advances,” *Advanced Materials*, vol. 24, no. 22, pp. 2945–2986, 2012, doi: 10.1002/adma.201103228.

[31] J. Raja *et al.,* “Improvement of Mobility in Oxide-Based Thin Film Transistors: A Brief Review,” *Transactions on Electrical and Electronic Materials*, vol. 16, no. 5, pp. 234–240, 2015, doi: 10.4313/TEEM.2015.16.5.234.

[32] Sungsik Lee and Arokia Nathan, “Subthreshold Schottky-barrier thin-film transistors with ultralow power and high intrinsic gain,” *Science*, vol. 354, no. 6310, pp. 302–304, 2016, doi: 10.1126/science.aah5035.

[33] A. K. Tripathi, K. Myny, B. Hou, K. Wezenberg, and G. H. Gelinck, “Electrical Characterization of Flexible InGaZnO Transistors and 8-b Transponder Chip Down to a Bending Radius of 2 mm,” *IEEE Transactions on Electron Devices*, vol. 62, no. 12, pp. 4063–4068, 2015, doi: 10.1109/TED.2015.2494694.

[34] P. Heremans *et al.,* “Mechanical and Electronic Properties of Thin-Film Transistors on Plastic, and Their Integration in Flexible Electronic Applications,” *Advanced Materials*, vol. 28, no. 22, pp. 4266–4282, 2016, doi: 10.1002/adma.201504360.

[35] D. Zhao, D. A. Mourey, and T. N. Jackson, “Fast Flexible Plastic Substrate ZnO Circuits,” *IEEE Electron Device Letters*, vol. 31, no. 4, pp. 323–325, 2010, doi: 10.1109/LED.2010.2041321.

[36] E. Fortunato, N. Correia, P. Barquinha, L. Pereira, G. Goncalves, and R. Martins, "High-Performance Flexible Hybrid Field-Effect Transistors Based on Cellulose Fiber Paper," *IEEE Electron Device Letters*, vol. 29, no. 9, pp. 988–990, 2008, doi: 10.1109/LED.2008.2001549.

[37] R. Martins *et al.,* "Selective floating gate non-volatile paper memory transistor," *physica status solidi (RRL) – Rapid Research Letters*, vol. 3, no. 9, pp. 308–310, 2009, doi: 10.1002/pssr.200903268.

[38] W. Lim *et al.,* "Low-voltage indium gallium zinc oxide thin film transistors on paper substrates," *Appl. Phys. Lett.*, vol. 96, no. 5, p. 53510, 2010, doi: 10.1063/1.3309753.

[39] R. F. P. Martins *et al.,* "Recyclable, Flexible, Low-Power Oxide Electronics," *Advanced Functional Materials*, vol. 23, no. 17, pp. 2153–2161, 2013, doi: 10.1002/adfm.201202907.

[40] Ick-Joon Park *et al.,* "Fabrication of amorphous InGaZnO thin-film transistor-driven flexible thermal and pressure sensors," *Semiconductor Science and Technology*, vol. 27, no. 10, p. 105019, 2012, doi: 10.1088/0268-1242/27/10/105019.

[41] Forough Mahmoudabadi, Xiaoxiao Ma, Miltiadis K. Hatalis, Kirit N. Shah, and Thomas L. Levendusky, "Amorphous IGZO TFTs and circuits on conformable aluminum substrates," *Solid-State Electronics*, vol. 101, pp. 57–62, 2014, doi: 10.1016/j.sse.2014.06.031.

[42] A. Plichta, A. Weber, and A. Habeck, "Ultra Thin Flexible Glass Substrates," *MRS Online Proceedings Library*, vol. 769, no. 1, p. 91, 2003, doi: 10.1557/PROC-769-H9.1.

[43] M.-K. Dai, J.-T. Lian, T.-Y. Lin, and Y.-F. Chen, "High-performance transparent and flexible inorganic thin film transistors: a facile integration of graphene nanosheets and amorphous InGaZnO," *J. Mater. Chem. C*, vol. 1, no. 33, pp. 5064–5071, 2013, doi: 10.1039/C3TC30890A.

[44] Gwang Jun Lee, Joonwoo Kim, Jung-Hye Kim, Soon Moon Jeong, Jae Eun Jang, and Jaewook Jeong, "High performance, transparent a-IGZO TFTs on a flexible thin glass substrate," *Semiconductor Science and Technology*, vol. 29, no. 3, p. 35003, 2014, doi: 10.1088/0268-1242/29/3/035003.

[45] Jin Zhang and Guo-Dong Wu, "Ultralow-Voltage Electric-Double-Layer Oxide-Based Thin-Film Transistors with Faster Switching Response on Flexible Substrates," *Chinese Physics Letters*, vol. 31, no. 7, p. 78502, 2014, doi: 10.1088/0256-307x/31/7/078502.

[46] Jin Zhang *et al.,* "Flexible Oxide-Based Thin-Film Transistors on Plastic Substrates for Logic Applications," *Journal of Materials Science & Technology*, vol. 31, no. 2, pp. 171–174, 2015, doi: 10.1016/j.jmst.2014.07.009.

[47] Mitsuru Nakata, Kazushige Takechi, Toshimasa Eguchi, Eisuke Tokumitsu, Hirotaka Yamaguchi, Setsuo Kaneko, "Effects of Thermal Annealing on ZnO Thin-Film Transistor Characteristics and the Application of Excimer Laser Annealing in Plastic-Based ZnO Thin-Film Transistors," *Japanese Journal of Applied Physics*, vol. 48, no. 8, p. 81608, 2009, doi: 10.1143/jjap.48.081608.

[48] D. Han *et al.,* "Flexible thin-film transistors on plastic substrate at room temperature," *Journal of Nanoscience and Nanotechnology*, vol. 13, no. 7, pp. 5154–5157, 2013.

[49] W. B. Jackson, R. L. Hoffman, and G. S. Herman, "High-performance flexible zinc tin oxide field-effect transistors," *Appl. Phys. Lett.*, vol. 87, no. 19, p. 193503, 2005, doi: 10.1063/1.2120895.

[50] H.-H. Hsieh, C.-H. Wu, C.-C. Wu, Y.-H. Yeh, H.-L. Tyan, and C.-M. Leu, "Amorphous In2O3-Ga2O3-ZnO Thin Film Transistors and Integrated Circuits on Flexible and Colorless Polyimide Substrates," *SID Symposium Digest of Technical Papers*, vol. 39, no. 1, pp. 1207–1210, 2008, doi: 10.1889/1.3069352.

[51] W. C. Sheets *et al.,* "Organic gate insulator materials for amorphous metal oxide TFTs," in *2015 IEEE 65th Electronic Components and Technology Conference (ECTC)*, 2015, pp. 1878–1882.

[52] Yun Cheol Kim, Su Jeong Lee, Il-Kwon Oh, Seunggi Seo, Hyungjun Kim, and Jae-Min Myoung, "Bending stability of flexible amorphous IGZO thin film transistors with transparent IZO/Ag/IZO oxide–metal–oxide electrodes," *Journal of Alloys and Compounds*, vol. 688, pp. 1108–1114, 2016, doi: 10.1016/j.jallcom.2016.07.169.

[53] P. Gao *et al.,* "Letter: Solution-processed flexible zinc-tin oxide thin-film transistors on ultra-thin polyimide substrates," *Journal of the Society for Information Display*, vol. 24, no. 4, pp. 211–215, 2016, doi: 10.1002/jsid.438.

[54] J.-I. Song *et al.,* "Transparent amorphous indium zinc oxide thin-film transistors fabricated at room temperature," *Appl. Phys. Lett.*, vol. 90, no. 2, p. 22106, 2007, doi: 10.1063/1.2430917.

[55] W. Lim *et al.,* "High-performance indium gallium zinc oxide transparent thin-film transistors fabricated by radio-frequency sputtering," *Journal of The Electrochemical Society*, vol. 155, no. 6, H383, 2008.

[56] Q. J. Yao and D. J. Li, "Fabrication and property study of thin film transistor using rf sputtered ZnO as channel layer," *Journal of non-crystalline solids*, vol. 351, 40-42, pp. 3191–3194, 2005.

[57] J. F. Wager, D. A. Keszler, and R. E. Presley, *Transparent electronics*: Springer, 2008.

[58] G. D. Wilk, R. M. Wallace, and J. Anthony, "High-κ gate dielectrics: Current status and materials properties considerations," *Journal of applied physics*, vol. 89, no. 10, pp. 5243–5275, 2001.

[59] J. Robertson and P. W. Peacock, "Electronic structure and band offsets of high-dielectric-constant gate oxides," in *High-κ Gate Dielectrics*: CRC Press, 2003, pp. 372–396.

[60] P. Barquinha *et al.,* "Low-temperature sputtered mixtures of high-κ and high bandgap dielectrics for GIZO TFTs," *Journal of the Society for Information Display*, vol. 18, no. 10, pp. 762–772, 2010, doi: 10.1889/JSID18.10.762.

[61] P. Barquinha *et al.,* "Gallium–Indium–Zinc-Oxide-Based Thin-Film Transistors: Influence of the Source/Drain Material," *IEEE Transactions on Electron Devices*, vol. 55, no. 4, pp. 954–960, 2008, doi: 10.1109/TED.2008.916717.

[62] J.-M. Kim *et al.,* "Atomic layer deposition ZnO: N flexible thin film transistors and the effects of bending on device properties," *Appl. Phys. Lett.*, vol. 98, no. 14, p. 142113, 2011.

[63] Y. Kumaresan *et al.,* "Highly bendable In-Ga-ZnO thin film transistors by using a thermally stable organic dielectric layer," *Scientific reports*, vol. 6, no. 1, pp. 1–10, 2016.

[64] J. Liu, D. B. Buchholz, J. W. Hennek, R. P. H. Chang, A. Facchetti, and T. J. Marks, "All-amorphous-oxide transparent, flexible thin-film transistors. Efficacy of bilayer gate dielectrics," *Journal of the American Chemical Society*, vol. 132, no. 34, pp. 11934–11942, 2010.

[65] C.-Y. Lee *et al.,* "Flexible ZnO transparent thin-film transistors by a solution-based process at various solution concentrations," *Semiconductor Science and Technology*, vol. 25, no. 10, p. 105008, 2010.

[66] H.-Y. Lee, W.-Y. Ye, Y.-H. Lin, L.-R. Lou, and C.-T. Lee, "High performance bottom-gate-type amorphous InGaZnO flexible transparent thin-film transistors deposited on PET substrates at low temperature," *Journal of electronic materials*, vol. 43, no. 3, pp. 780–785, 2014.

[67] A. E. H. Love, *A treatise on the mathematical theory of elasticity*: Cambridge University Press, 2013.

[68] R. J. Young and P. A. Lovell, *Introduction to polymers*: CRC Press, 2011.

[69] T. P. Weihs, S. Hong, J. C. Bravman, and W. D. Nix, "Mechanical deflection of cantilever microbeams: A new technique for testing the mechanical properties of thin films," *J. Mater. Res.*, vol. 3, no. 5, pp. 931–942, 1988.

[70] M. F. Doerner and W. D. Nix, "A method for interpreting the data from depth-sensing indentation instruments," *J. Mater. Res.*, vol. 1, no. 4, pp. 601–609, 1986, doi: 10.1557/JMR.1986.0601.

[71] W. C. Oliver and G. M. Pharr, "An improved technique for determining hardness and elastic modulus using load and displacement sensing indentation experiments," *J. Mater. Res.*, vol. 7, no. 6, pp. 1564–1583, 1992, doi: 10.1557/JMR.1992.1564.

[72] D. Tabor, "A simple theory of static and dynamic hardness," *Proc. R. Soc. Lond. A*, vol. 192, no. 1029, pp. 247–274, 1948, doi: 10.1098/rspa.1948.0008.

[73] Ian N. Sneddon, "The relation between load and penetration in the axisymmetric boussinesq problem for a punch of arbitrary profile," *International Journal of Engineering Science*, vol. 3, no. 1, pp. 47–57, 1965, doi: 10.1016/0020-7225(65)90019-4.

[74] A. Chakravartula and K. Komvopoulos, "Viscoelastic properties of polymer surfaces investigated by nanoscale dynamic mechanical analysis," *Appl. Phys. Lett.*, vol. 88, no. 13, p. 131901, 2006, doi: 10.1063/1.2189156.

[75] A. C. Fischer-Cripps, *Nanoindentation,* 3rd ed. New York: Springer, 2011.

[76] R. Saha and W. D. Nix, "Effects of the substrate on the determination of thin film mechanical properties by nanoindentation," *Acta Materialia*, vol. 50, no. 1, pp. 23–38, 2002, doi: 10.1016/S1359-6454(01)00328-7.

[77] G. Marchiori *et al.,* "Optimizing thickness of ceramic coatings on plastic components for orthopedic applications: A finite element analysis," *Materials Science and Engineering: C*, vol. 58, pp. 381–388, 2016, doi: 10.1016/j.msec.2015.08.067.

[78] A. Rudin and P. Choi, Eds., *The Elements of Polymer Science & Engineering (Third Edition)*. Boston: Academic Press, 2013.

[79] S. K. Lee, Y. R. Kim, S. H. Kim, and J. H. Kim, "Investigation of the internal stress relaxation in FDM 3D printing: Annealing conditions," *Journal of the Korean Society of Manufacturing Process Engineers*, vol. 17, no. 4, pp. 130–136, 2018.

[80] Y. Liao *et al.,* "Effect of Porosity and Crystallinity on 3D Printed PLA Properties," *Polymers*, vol. 11, no. 9, 2019, doi: 10.3390/polym11091487.

[81] W. C. Oliver and G. M. Pharr, "Measurement of hardness and elastic modulus by instrumented indentation: Advances in understanding and refinements to methodology," *J. Mater. Res.*, vol. 19, no. 1, pp. 3–20, 2004, doi: 10.1557/jmr.2004.19.1.3.

[82] A. Clausner, S. Schlipf, C. Sander, R. Schwerz, and M. Roellig, "Macro- and Microscopic DMA measurements - Complementary techniques to determine viscoelastic material properties of packaging polymers," in *2022 23rd International Conference on Thermal, Mechanical and Multi-Physics Simulation and Experiments in Microelectronics and Microsystems (EuroSimE)*, 2022, pp. 1–6.

[83] Douglas Altman, David Machin, Trevor Bryant, Martin Gardner, *Statistics with Confidence: Confidence Intervals and Statistical Guidelines,* 2nd ed.: BMJ Books, 2000.

[84] M. L. Slanik, J. A. Nemes, M.-J. Potvin, and J.-C. Piedboeuf, "Time Domain Finite Element Simulations of Damped Multilayered Beams Using a Prony Series Representation," *Mechanics of Time-Dependent Materials*, vol. 4, no. 3, pp. 211–230, 2000, doi: 10.1023/A:1009826923983.

[85] S. W. Park and R. A. Schapery, "Methods of interconversion between linear viscoelastic material functions. Part I—a numerical method based on Prony series," *International Journal of Solids and Structures*, vol. 36, no. 11, pp. 1653–1675, 1999, doi: 10.1016/S0020-7683(98)00055-9.

[86] R. A. Schapery and S. W. Park, "Methods of interconversion between linear viscoelastic material functions. Part II—an approximate analytical method," *International Journal of Solids and Structures*, vol. 36, no. 11, pp. 1677–1699, 1999, doi: 10.1016/S0020-7683(98)00060-2.

[87] E. W. Fischer, "Effect of annealing and temperature on the morphological structure of polymers," vol. 31, 1-2, pp. 113–132, 1972, doi: 10.1351/pac197231010113.

[88] G. M. Pharr, E. G. Herbert, and Y. Gao, "The Indentation Size Effect: A Critical Examination of Experimental Observations and Mechanistic Interpretations," *Annual Review of Materials Research*, vol. 40, no. 1, pp. 271–292, 2010, doi: 10.1146/annurev-matsci-070909-104456.

[89] L. B. Freund and S. Suresh, *Thin film materials: stress, defect formation and surface evolution*: Cambridge University Press, 2004.

[90] Y. Choi, J. Park, and H. Shin, "New Simulation Method for Dependency of Device Degradation on Bending Direction and Channel Length," *Materials*, vol. 14, no. 20, p. 6167, 2021.

[91] J. A. Shields, *Applications of Molybdenum Metal and Its Alloys*.

[92] P. Shang, S. Xiong, L. Li, D. Tian, and W. Ai, "Investigation on thermal stability of Ta2O5, TiO2 and Al2O3 coatings for application at high temperature," *Applied Surface Science*, vol. 285, pp. 713–720, 2013, doi: 10.1016/j.apsusc.2013.08.115.

[93] L. Šimurka, R. Čtvrtlík, J. Tomaštík, G. Bektaş, J. Svoboda, and K. Bange, "Mechanical and optical properties of SiO2 thin films deposited on glass," *Chemical Papers*, vol. 72, no. 9, pp. 2143–2151, 2018, doi: 10.1007/s11696-018-0420-z.

A

APPENDIX: TABLES

A.1 Thickness Measurements

Table A.1 – Average thickness obtained from profilometry in comparison to the desired thickness.

Material	Number of measurements	Average thickness	Desired thickness
Mo	9	39.5 ± 2.3 nm	100 nm
		180.1 ± 3.7 nm	200 nm
		438.6 ± 3.7 nm	500 nm
IGZO	9	134.8 ± 2.7 nm	100 nm
		261.2 ± 2.8 nm	200 nm
		608.6 ± 4.8 nm	500 nm
Ta_2O_5	3	311.9 ± 4.8 nm	350 nm
Ta_2O_5/SiO_2	3	343.3 ± 4.3 nm	370 nm
Polyimide (250 °C)	3	1.100 ± 0.016 µm	500 nm
		1.583 ± 0.005 µm	1 µm
		10.153 ± 0.151 µm	10 µm
Polyimide (350 °C)	3	1.066 ± 0.004 µm	500 nm
		1.563 ± 0.002 µm	1 µm
		9.516 ± 0.330 µm	10 µm

B

APPENDIX: FIGURES

B.1 SEM cross-sections for Ta_2O_5 and Ta_2O_5/SiO_2

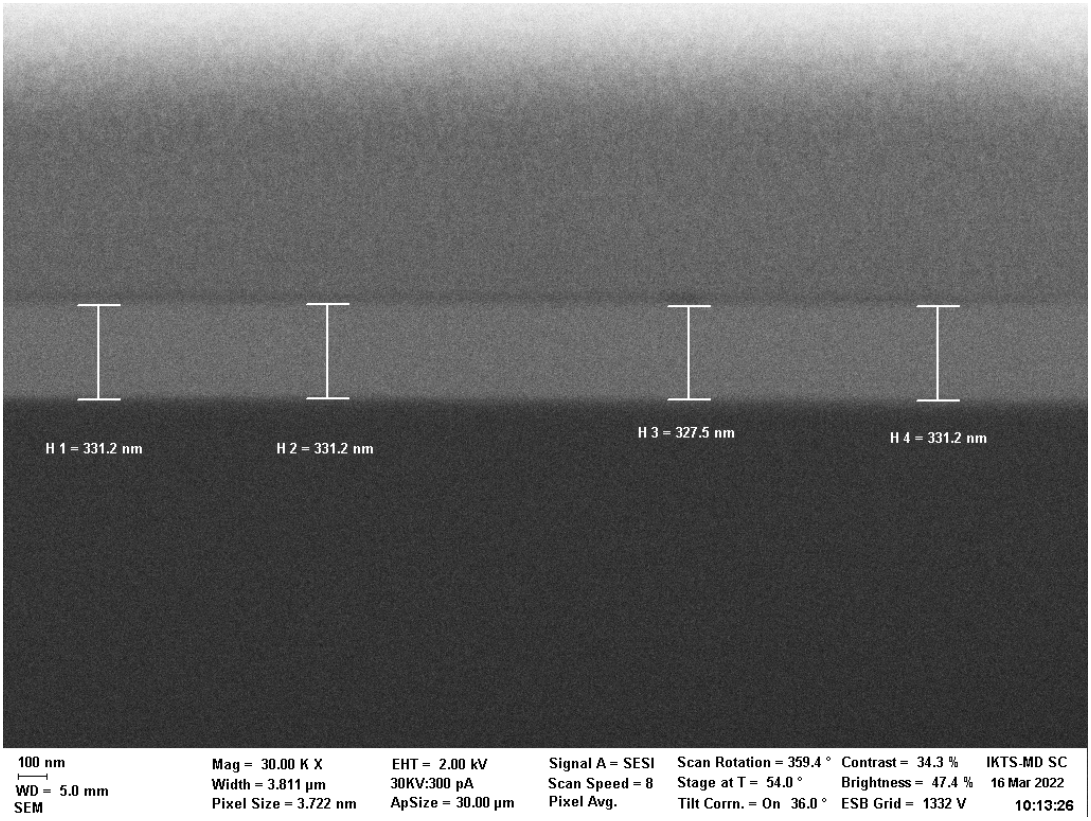

Figure B.1.1 — SEM cross-section for Ta_2O_5 as deposited, with 4 thickness measurements.

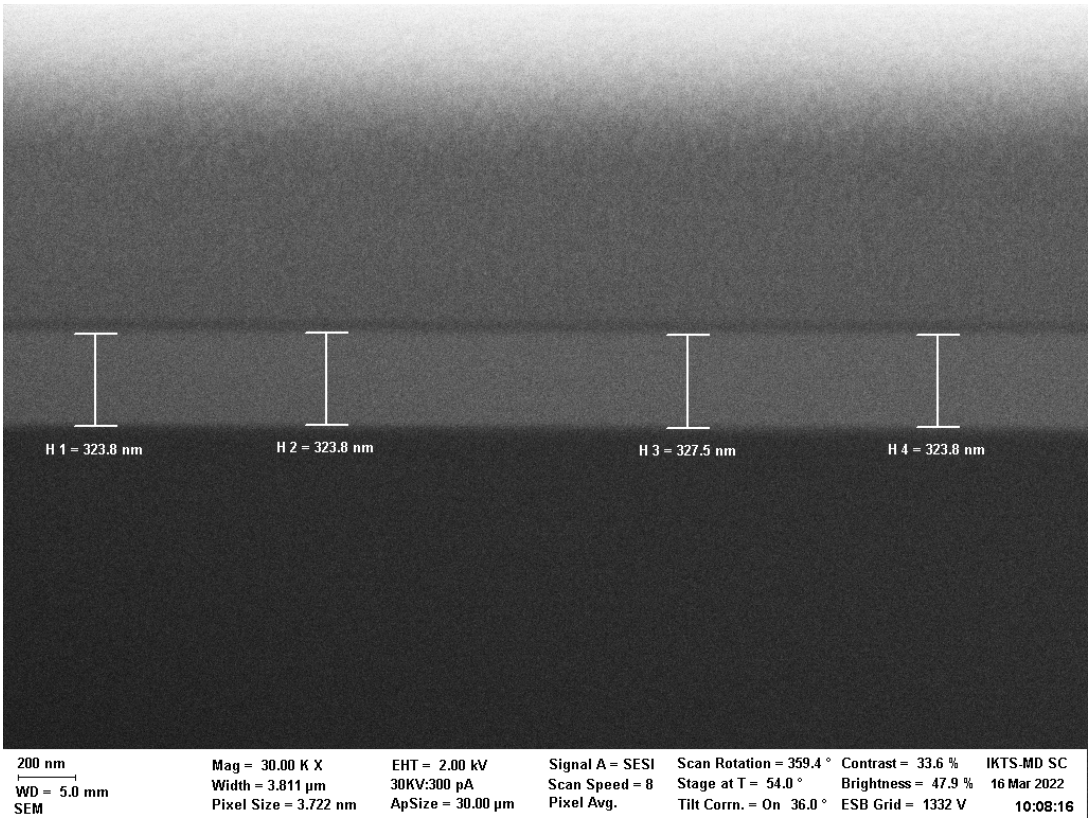

Figure B.1.2 — SEM cross-section for Ta_2O_5 as deposited, with 4 thickness measurements.

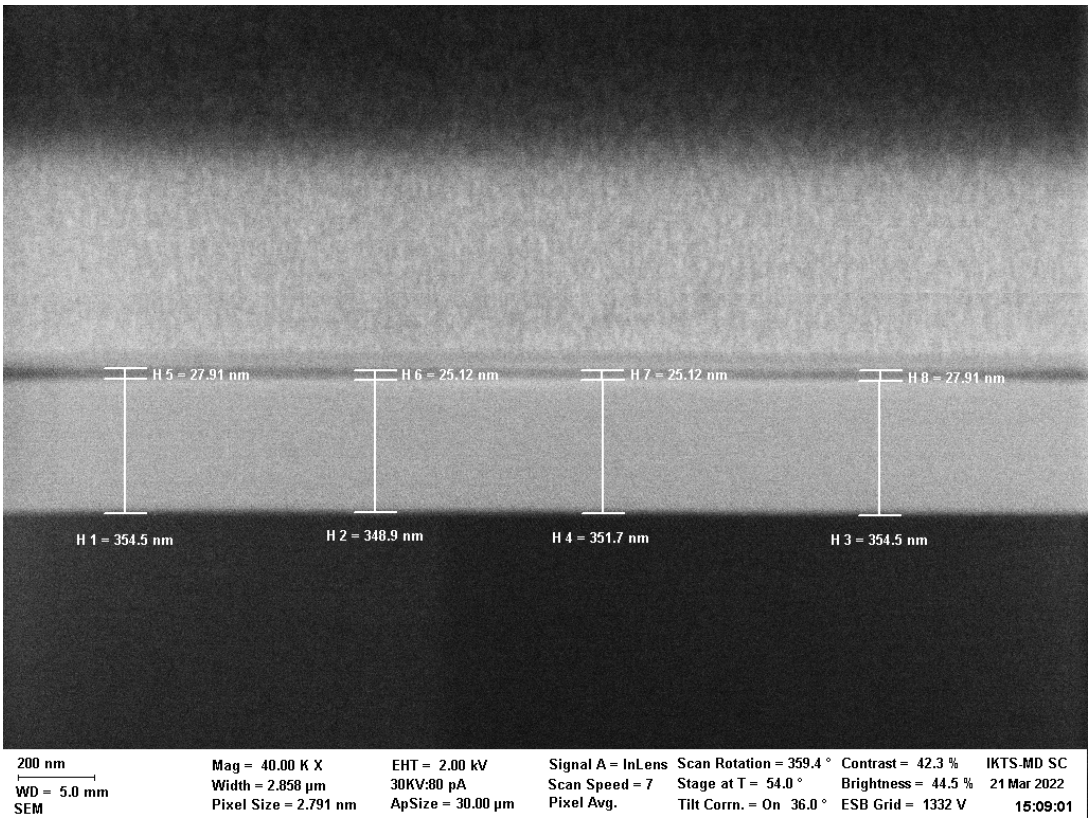

Figure B.1.3 — SEM cross-section for Ta_2O_5/SiO_2 as deposited, with 8 thickness measurements.

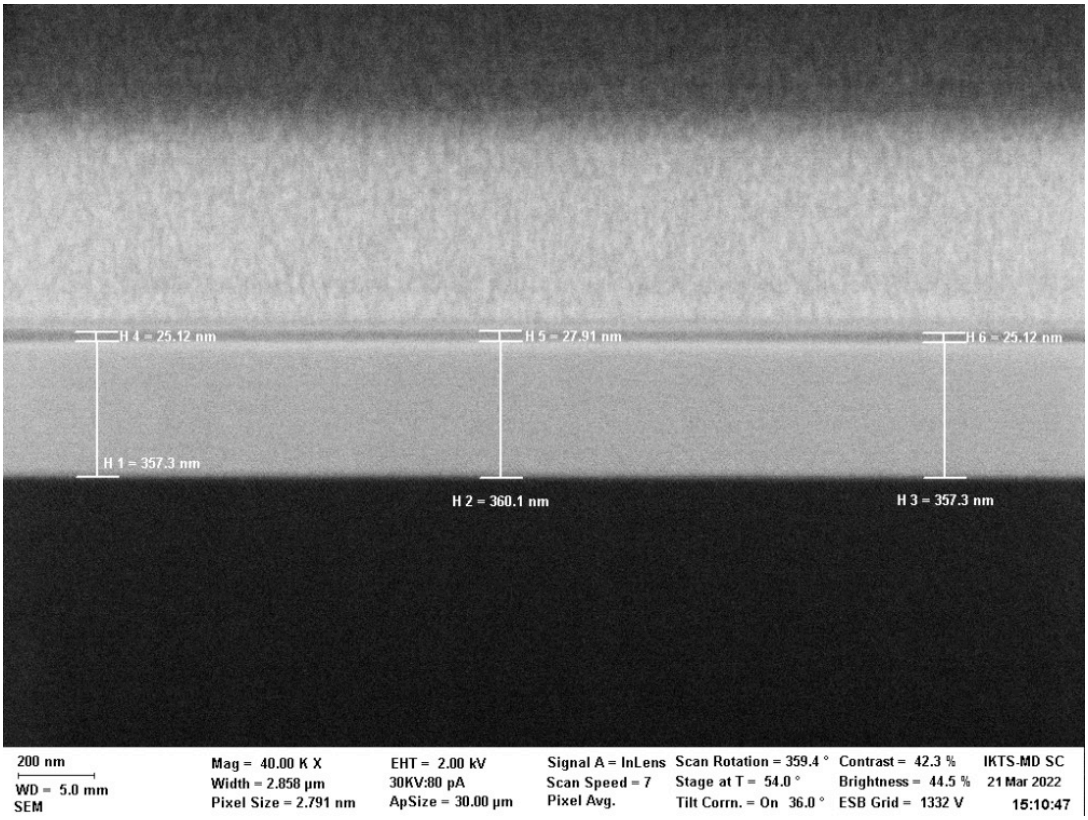

Figure B.1.4 — SEM cross-section for Ta_2O_5/SiO_2 as deposited, with 8 thickness measurements.

B.2 EDS

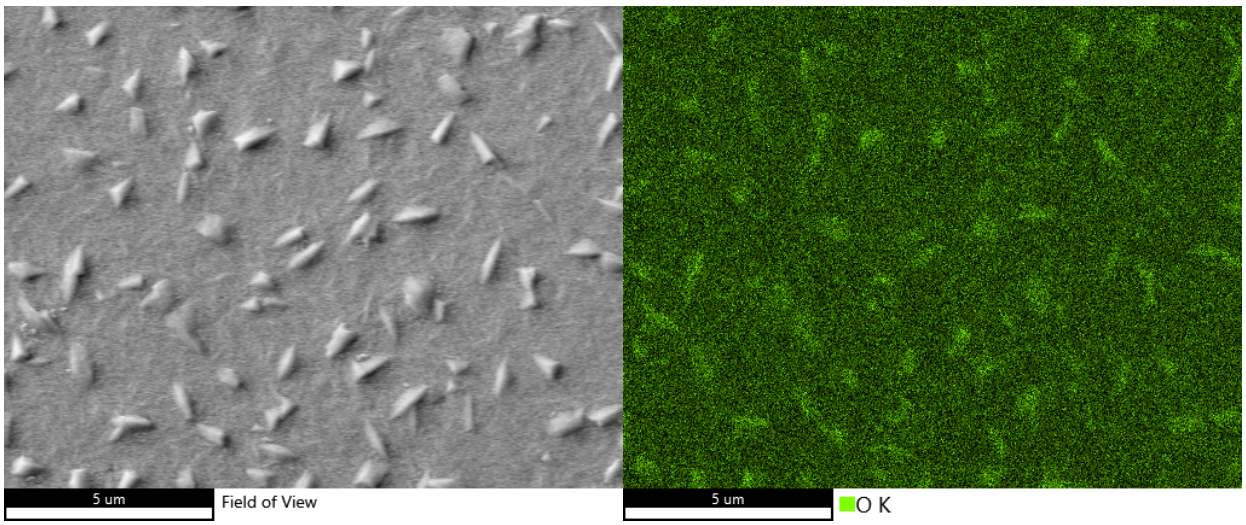

Figure B.2.1 — SEM image, energy dispersive X-ray (EDS) elemental mapping of (right) O.

B.3 Quasi-Static Nanoindentation Measurements for IGZO

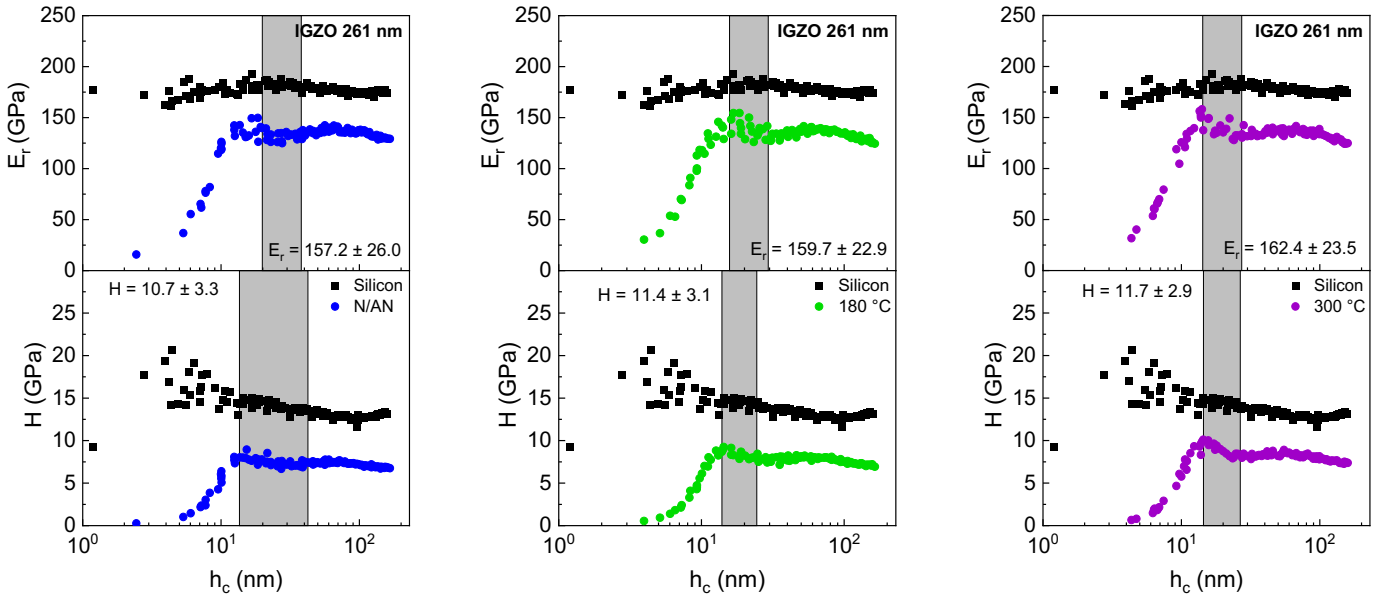

Figure B.3.1 — Nanoindentation measurements for Young's modulus and hardness for IGZO with a thickness of 261 nm: (left) as deposited; (centre) annealed at 180 ºC; (right) annealed at 300 ºC.

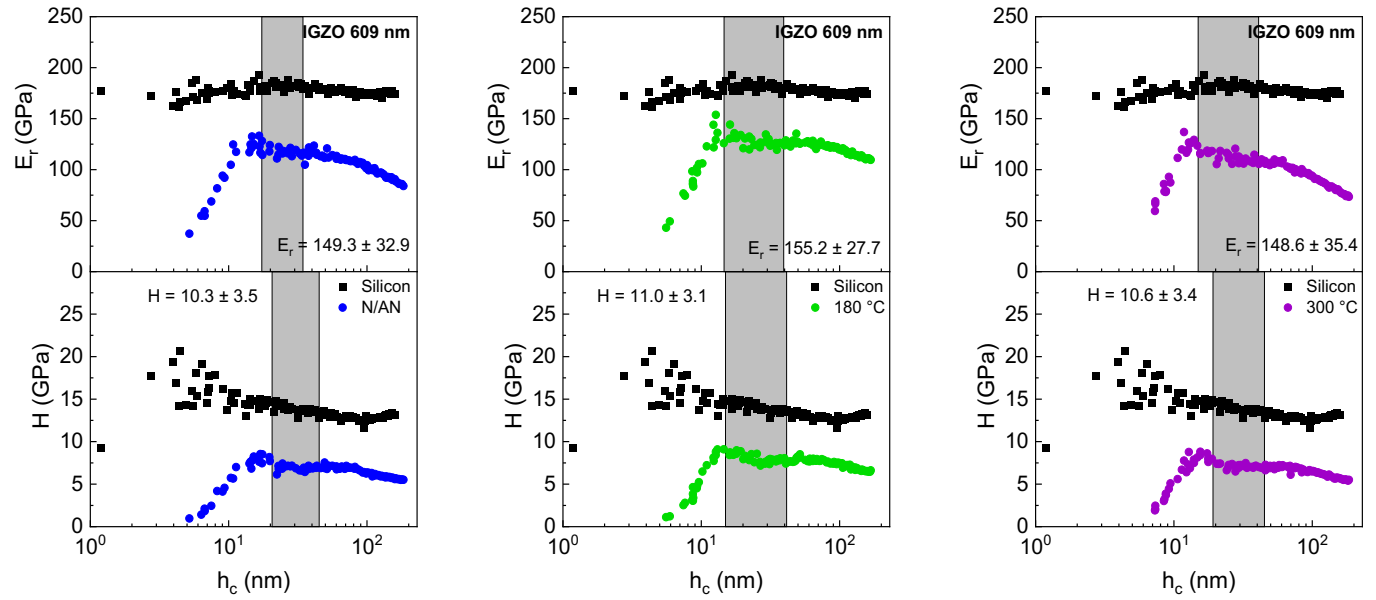

Figure B.3.2 — Nanoindentation measurements for Young's modulus and hardness for IGZO with a thickness of 609 nm: (left) as deposited; (centre) annealed at 180 ºC; (right) annealed at 300 ºC.

B.4 Quasi-Static Nanoindentation Measurements for Ta_2O_5 and Multilayer Stack (Ta_2O_5/SiO_2)

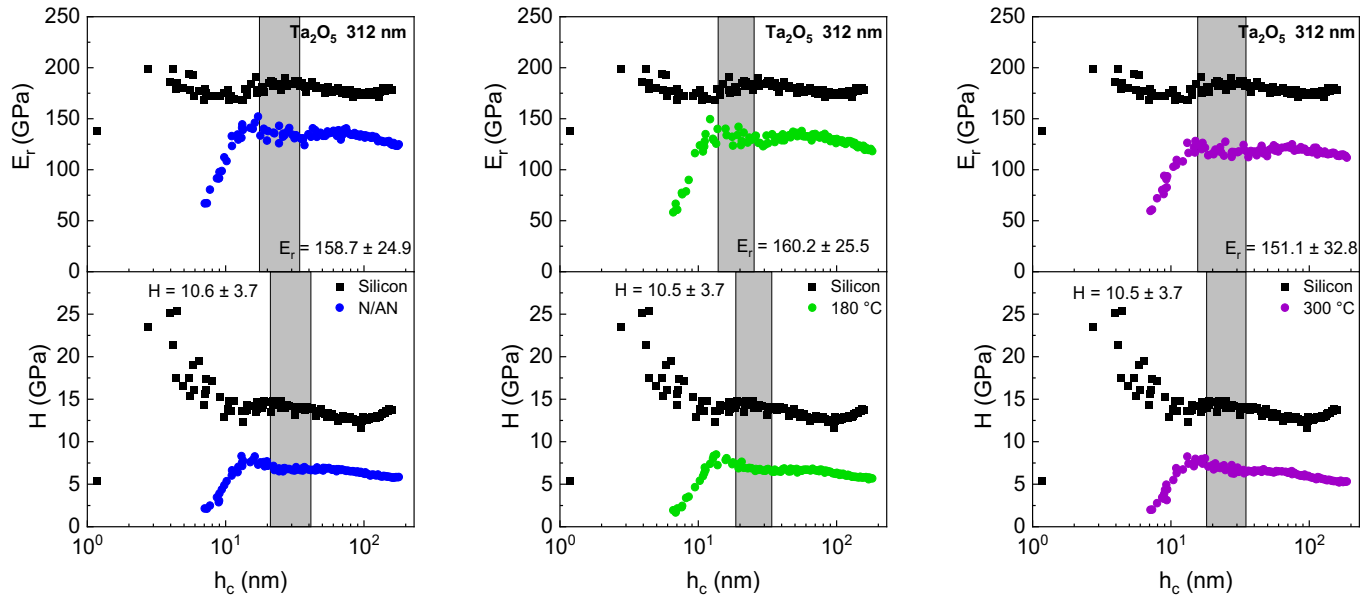

Figure B.4.1 — Nanoindentation measurements of Young's modulus and hardness for Ta_2O_5 with a thickness of 312 nm: (left) as deposited; (centre) annealed at 180 ºC; (right) annealed at 300 ºC.

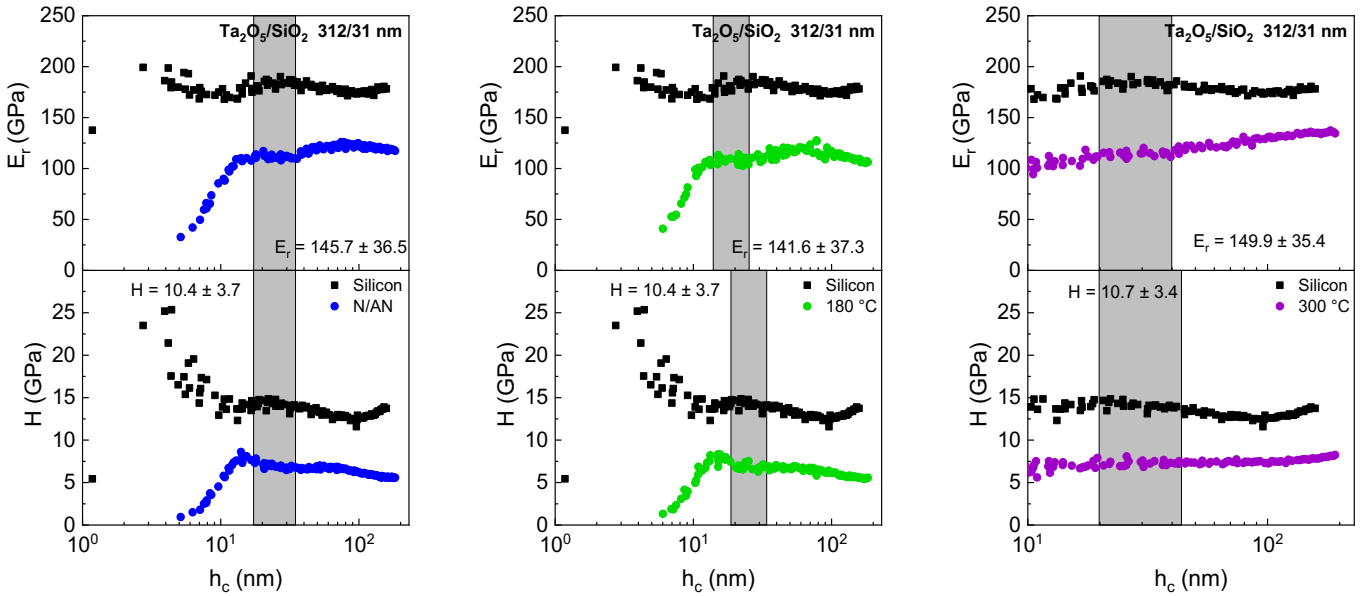

Figure B.4.2 — Nanoindentation measurements of Young's modulus and hardness for Ta_2O_5/SiO_2 with a thickness of 312/31 nm: (left) as deposited; (centre) annealed at 180 ºC; (right) annealed at 300 ºC.

B.5 Quasi-Static Nanoindentation Measurements for PI

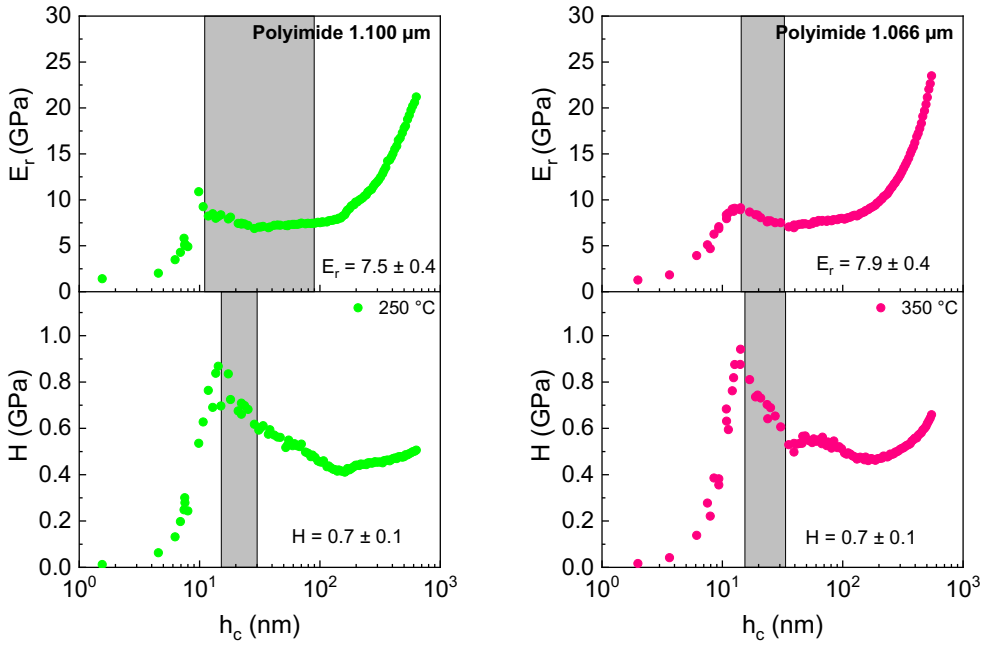

Figure B.5.1 — Nanoindentation measurements for Young's modulus and hardness for PI with a thickness of: (left) 1.100 µm annealed at 250 ºC; (right) 1.066 µm annealed at 300 ºC.

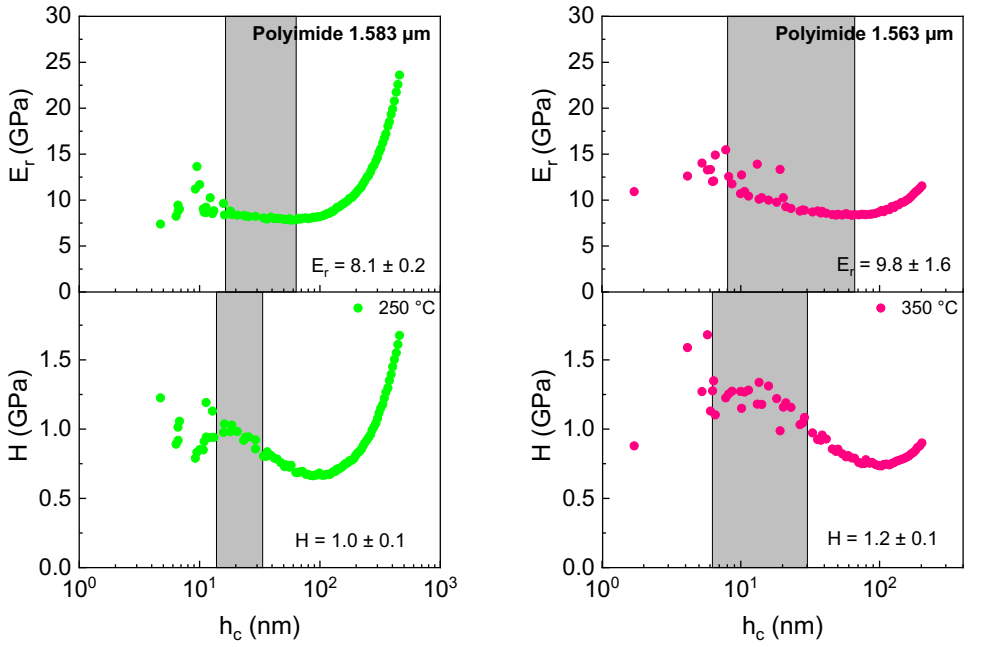

Figure B.5.2 — Nanoindentation measurements for Young's modulus and hardness for PI with a thickness of: (left) 1.583 µm annealed at 250 ºC; (right) 1.563 µm annealed at 300 ºC.

B.6 Nano-DMA Measurements of Storage Modulus for PI

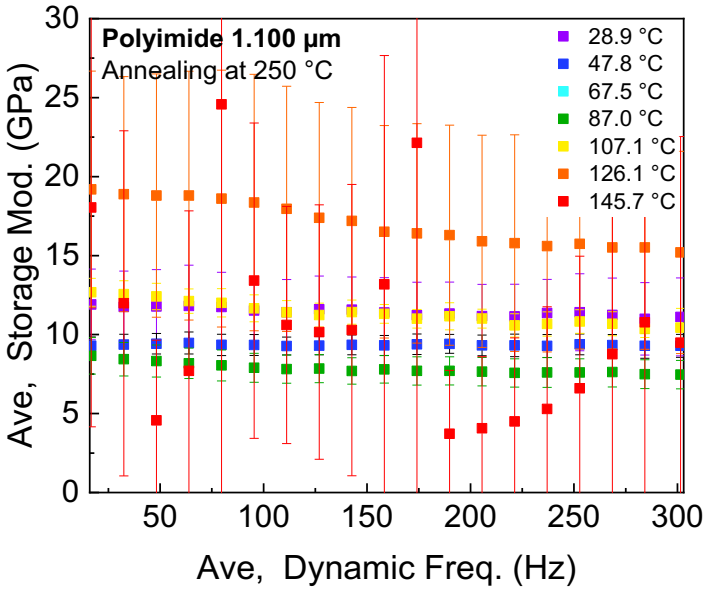

Figure B.6.1 — Nano-DMA measurements of storage modulus vs frequency at different temperatures for PI with a thickness of 1.100 µm annealed at 250 ºC.

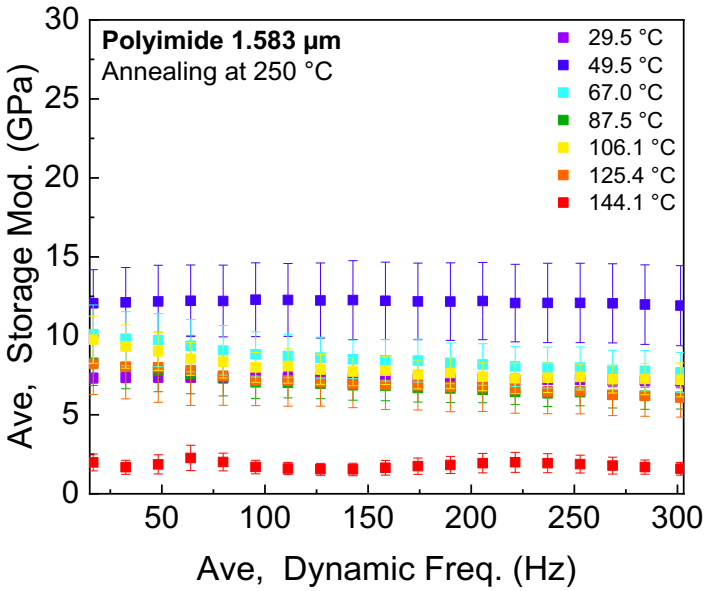

Figure B.6.2 — Nano-DMA measurements of storage modulus vs frequency at different temperatures for PI with a thickness of 1.583 µm annealed at 250 ºC.

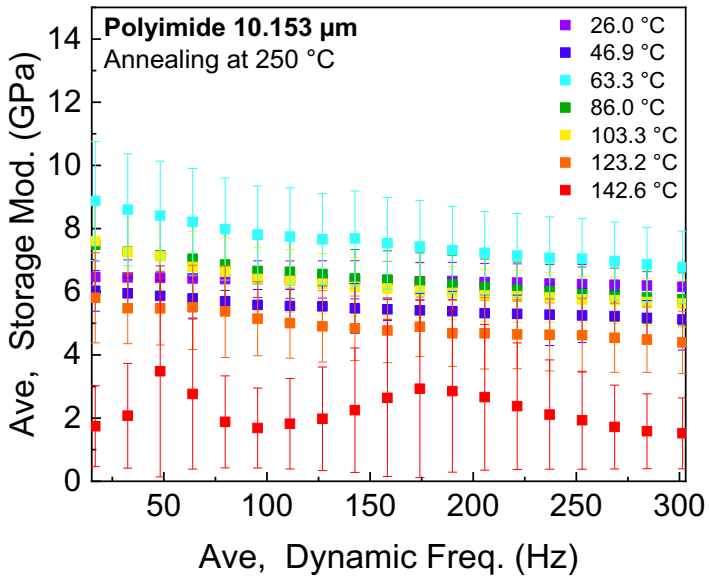

Figure B.6.3— Nano-DMA measurements of storage modulus vs frequency at different temperatures for PI with a thickness of 10.153 µm annealed at 250 ºC.

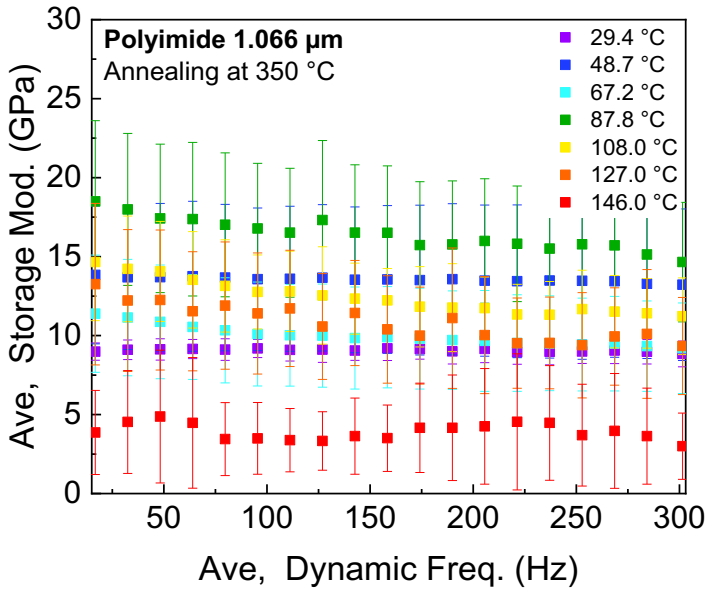

Figure B.6.4 — Nano-DMA measurements of storage modulus vs frequency at different temperatures for PI with a thickness of 1.066 µm annealed at 350 ºC.

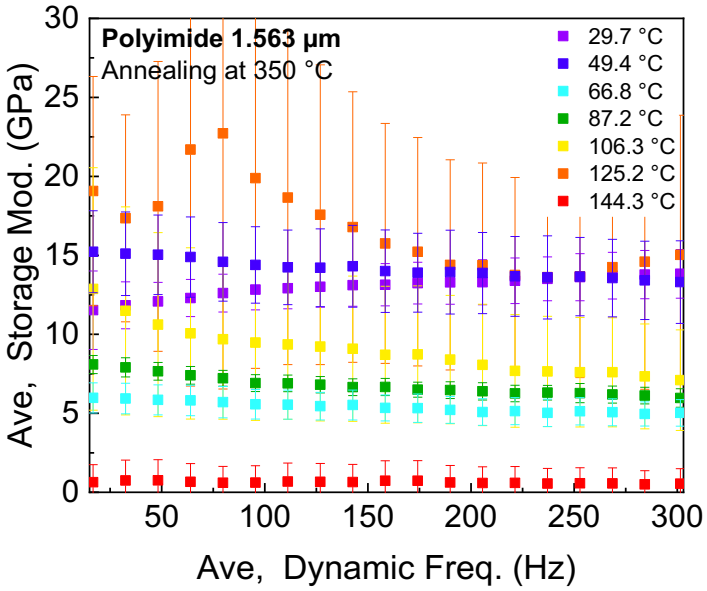

Figure B.6.5 — Nano-DMA measurements of storage modulus vs frequency at different temperatures for PI with a thickness of 1.563 µm annealed at 350 ºC.

B.7 Nano-DMA Measurements of Storage Modulus for PI

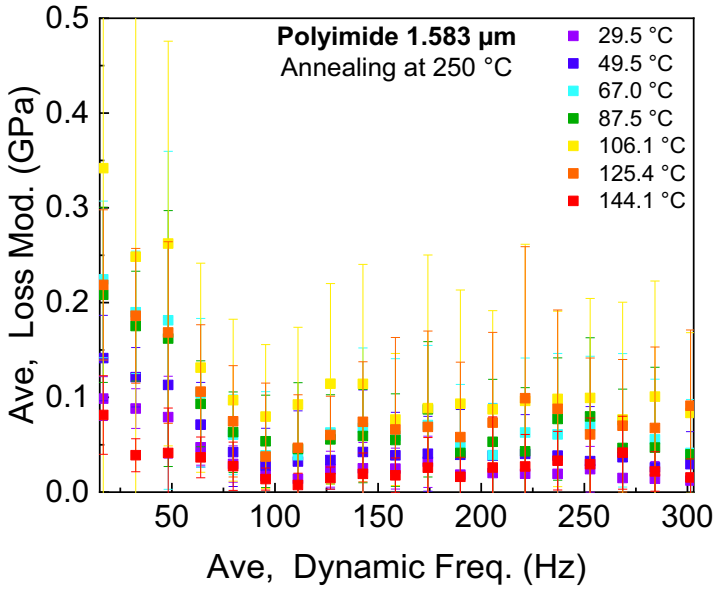

Figure B.7.1 — Nano-DMA measurements of loss modulus vs frequency at different temperatures for PI with a thickness of 1.583 µm annealed at 250 ºC.

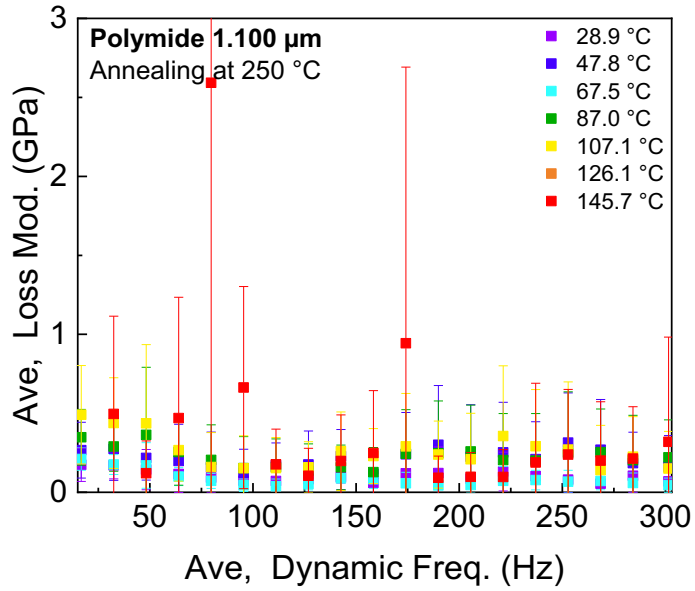

Figure B.7.2 — Nano-DMA measurements of loss modulus vs frequency at different temperatures for PI with a thickness of 1.100 µm annealed at 250 ºC.

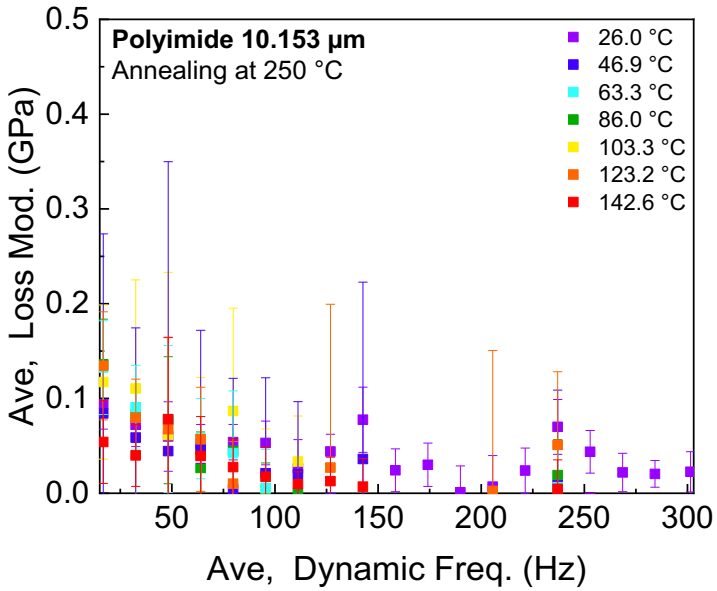

Figure B.7.3 — Nano-DMA measurements of loss modulus vs frequency at different temperatures for PI with a thickness of 10.153 µm annealed at 250 ºC.

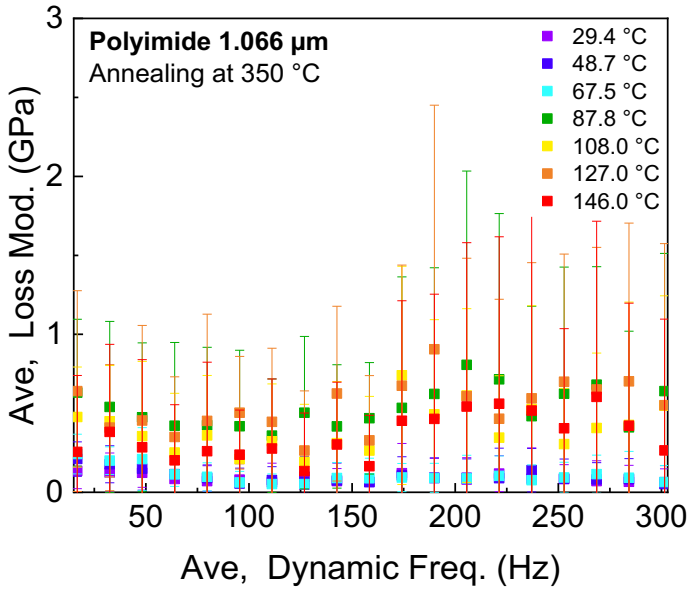

Figure B.7.4 — Nano-DMA measurements of loss modulus vs frequency at different temperatures for PI with a thickness of 1.066 µm annealed at 350 ºC.

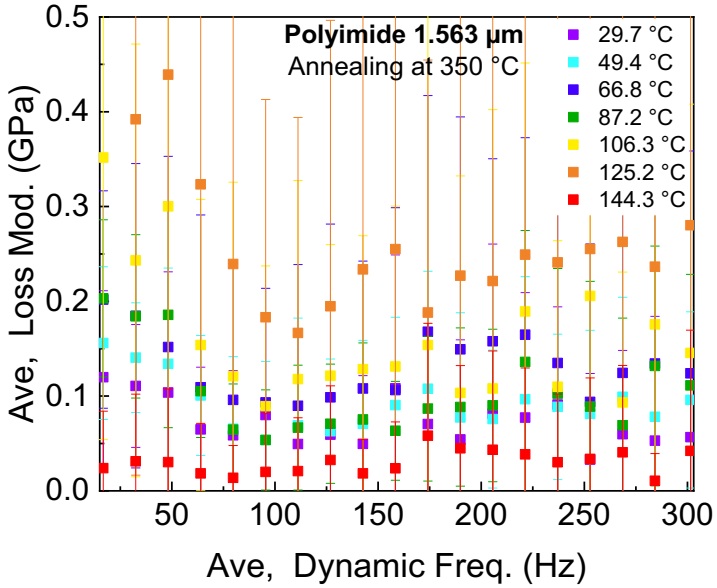

Figure B.7.5 — Nano-DMA measurements of loss modulus vs frequency at different temperatures for PI with a thickness of 1.563 µm annealed at 350 ºC.

B.8 Nano-DMA Measurements of Phase Angle for PI

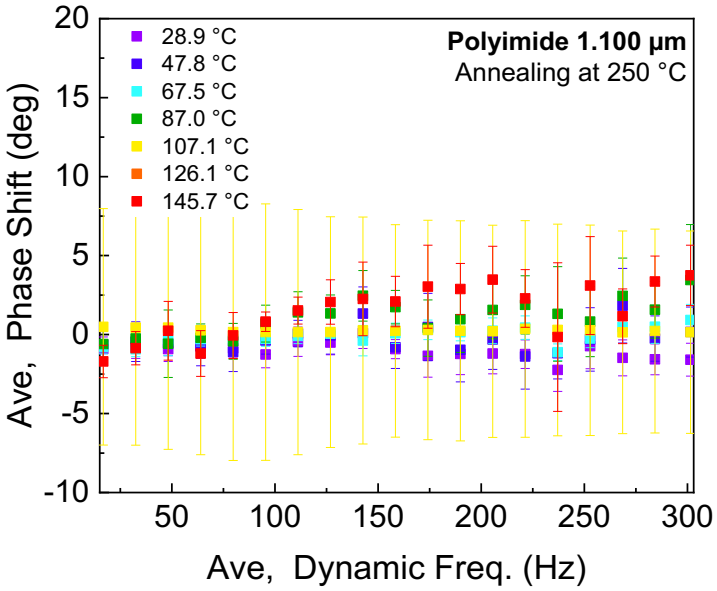

Figure B.8.1 — Nano-DMA measurements of phase shift vs frequency at different temperatures for PI with a thickness of 1.100 µm annealed at 250 ºC.

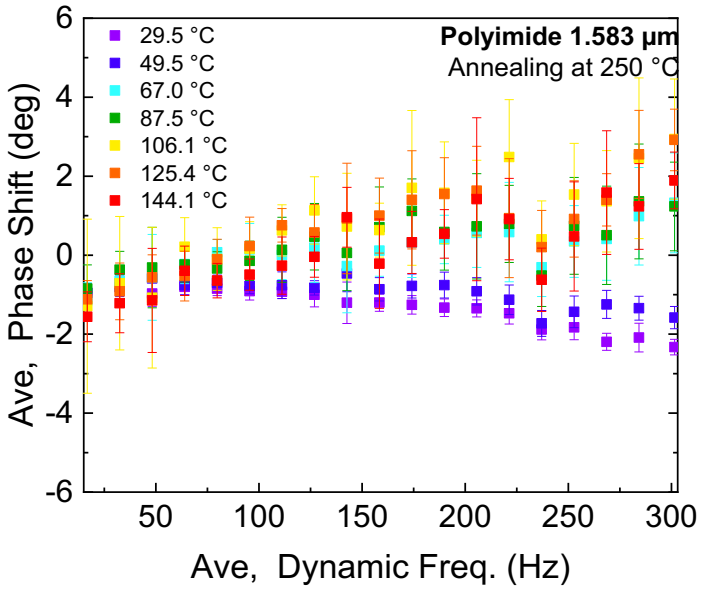

Figure B.8. 2 — Nano-DMA measurements of phase shift vs frequency at different temperatures for PI with a thickness of 1.583 µm annealed at 250 ºC.

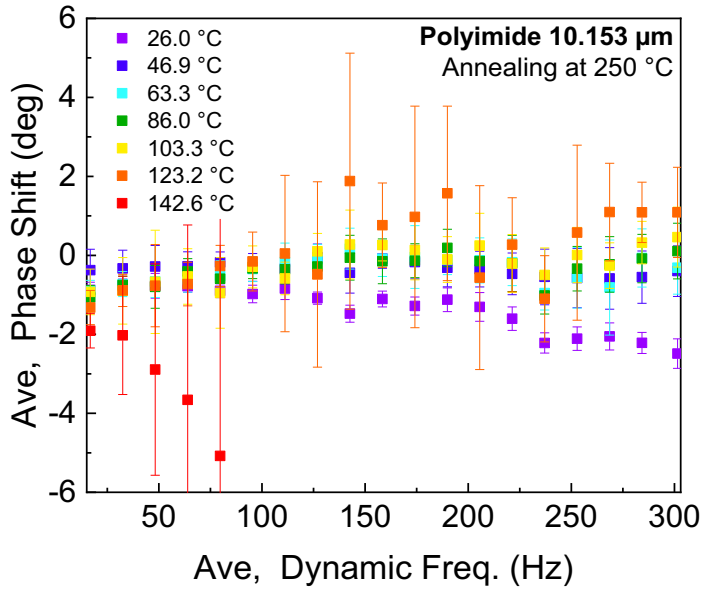

Figure B.8.3 — Nano-DMA measurements of phase shift vs frequency at different temperatures for PI with a thickness of 10.153 µm annealed at 250 ºC.

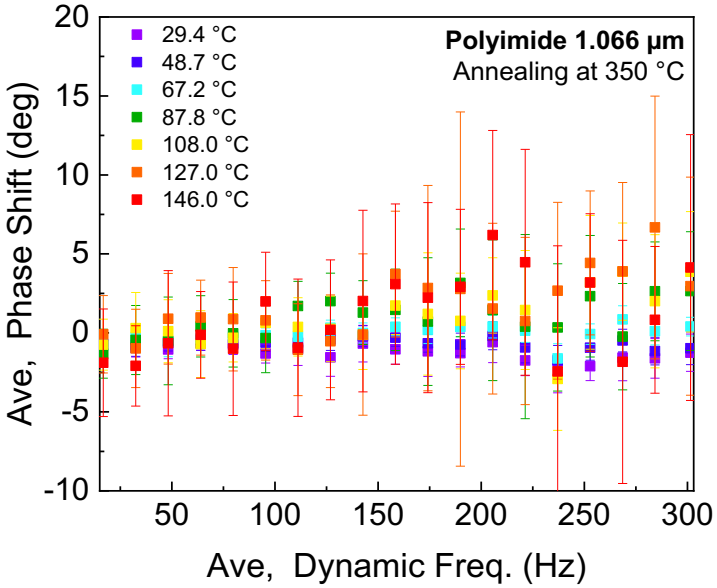

Figure B.8.4 — Nano-DMA measurements of phase shift vs frequency at different temperatures for PI with a thickness of 1.066 µm annealed at 350 ºC.

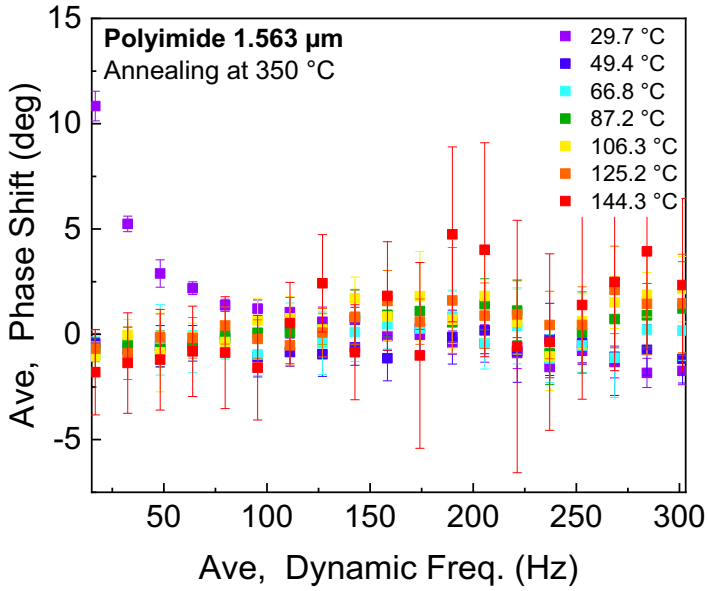

Figure B.8.5 — Nano-DMA measurements of phase shift vs frequency at different temperatures for PI with a thickness of 1.563 µm annealed at 350 ºC.